

1 SEARCH FOR  $t\bar{t}Z' \rightarrow t\bar{t}t\bar{t}$  PRODUCTION IN THE MULTILEPTON FINAL STATE IN  
2  $pp$  COLLISIONS AT  $\sqrt{s} = 13$  TEV WITH THE ATLAS DETECTOR

By

Hieu Le

## A DISSERTATION

Submitted to  
Michigan State University  
in partial fulfillment of the requirements  
for the degree of

## Physics — Doctor of Philosophy

2025

## ABSTRACT

13 Lorem ipsum dolor sit amet, consectetur adipiscing elit, sed do eiusmod tempor incididunt ut  
14 labore et dolore magna aliqua. Ut enim ad minim veniam, quis nostrud exercitation ullamco  
15 laboris nisi ut aliquip ex ea commodo consequat. Duis aute irure dolor in reprehenderit in  
16 voluptate velit esse cillum dolore eu fugiat nulla pariatur. Excepteur sint occaecat cupidatat  
17 non proident, sunt in culpa qui officia deserunt mollit anim id est laborum.

## ACKNOWLEDGMENTS

- <sup>19</sup> Advisor: Reinhard Schwienhorst
- <sup>20</sup> Postdoc: Binbin Dong
- <sup>21</sup> Committee
- <sup>22</sup> MSU group
- <sup>23</sup> ATLAS analysis group
- <sup>24</sup> Friend: Daniel, Grayson, Bella, Eric, Jordan
- <sup>25</sup> Other friends: Jasper, Adam, Brittany
- <sup>26</sup> Parents
- <sup>27</sup> Spouse: Allen Sechrist
- <sup>28</sup> ATLAS in general & funding agencies

## PREFACE

<sup>30</sup> This is my preface. remarks remarks remarks

## TABLE OF CONTENTS

31	<b>List of Tables</b>	vii
32	<b>List of Figures</b>	viii
33	<b>KEY TO ABBREVIATIONS</b>	ix
34	<b>Roadmap</b>	1
35	<b>Chapter 1. Introduction</b>	2
36	<b>Chapter 2. Theoretical Overview</b>	3
37	2.1 The Standard Model	3
38	2.1.1 Elementary particles	3
39	2.1.2 Mathematical formalism	6
40	2.1.3 Shortcomings of the Standard Model	16
41	2.2 Beyond the Standard Model	16
42	2.2.1 Top-philic vector resonance	16
43	2.3 Four-top quark production	18
44	<b>Chapter 3. LHC &amp; ATLAS Experiment</b>	21
45	3.1 The Large Hadron Collider	21
46	3.1.1 Overview	21
47	3.1.2 LHC operations	21
48	3.2 The ATLAS detector	24
49	3.2.1 Inner detector	24
50	3.2.2 Calorimeter systems	26
51	3.2.3 Muon spectrometer	27
52	3.2.4 Forward detectors	29
53	3.2.5 Magnetic systems	29
54	3.2.6 Trigger & data acquisition	29
55	<b>Chapter 4. Data &amp; Simulated Samples</b>	31
56	4.1 Data samples	31
57	4.2 Monte Carlo samples	32
58	4.2.1 $t\bar{t}Z'$ signal samples	32
59	4.2.2 Background samples	32
60	<b>Chapter 5. Particle Reconstruction &amp; Identification</b>	34
61	5.1 Primary reconstruction	34
62	5.1.1 Topological clusters	34
63	5.1.2 Tracks	35
64	5.1.3 Vertices	36

65	5.2	Jets . . . . .	37
66	5.2.1	Flavor tagging . . . . .	38
67	5.3	Leptons . . . . .	41
68	5.3.1	Electrons . . . . .	41
69	5.3.2	Muons . . . . .	45
70	5.4	Missing transverse momentum . . . . .	47
71	5.5	Overlap removal . . . . .	49
72	5.6	Object definition . . . . .	49
73	<b>Chapter 6. Analysis Strategy</b> . . . . .	<b>51</b>	
74	6.1	Event selection . . . . .	51
75	6.2	Analysis regions . . . . .	53
76	6.2.1	Signal regions . . . . .	54
77	6.2.2	Control regions . . . . .	54
78	6.2.3	Validation regions . . . . .	56
79	6.3	Background estimation . . . . .	57
80	6.3.1	Template fitting for fake/non-prompt estimation . . . . .	59
81	6.3.2	Charge misidentification data-driven estimation . . . . .	60
82	6.3.3	$t\bar{t}W$ background data-driven estimation . . . . .	61
83	<b>Chapter 7. Systematic Uncertainties</b> . . . . .	<b>65</b>	
84	7.1	Experimental uncertainties . . . . .	65
85	7.1.1	Leptons . . . . .	65
86	7.1.2	Jets . . . . .	66
87	7.1.3	Missing transverse energy . . . . .	68
88	7.2	Modeling uncertainties . . . . .	68
89	7.2.1	Signal and irreducible background uncertainties . . . . .	68
90	7.2.2	Reducible background uncertainties . . . . .	71
91	<b>Chapter 8. Results</b> . . . . .	<b>74</b>	
92	8.1	Statistical model . . . . .	74
93	8.1.1	Binned profile likelihood fit . . . . .	74
94	8.1.2	Signal significance . . . . .	74
95	8.1.3	Limit exclusion . . . . .	74
96	8.2	Fit results . . . . .	74
97	8.3	Limits . . . . .	75
98	<b>Chapter 9. Summary</b> . . . . .	<b>76</b>	
99	<b>References</b> . . . . .	<b>77</b>	

# <sup>100</sup> List of Tables

<sup>101</sup> Table 4.1: Caption . . . . .	31
<sup>102</sup> Table 4.2: Summary of all Monte-Carlo samples used in this analysis. . . . .	33
<sup>103</sup> Table 5.1: Caption . . . . .	49
<sup>104</sup> Table 5.2: Caption . . . . .	50
<sup>105</sup> Table 6.1: Caption . . . . .	54
<sup>106</sup> Table 6.2: Caption . . . . .	55
<sup>107</sup> Table 6.3: Caption . . . . .	58
<sup>108</sup> Table 7.1: Summary of the experimental systematic uncertainties considered in this <sup>109</sup> analysis. . . . .	69
<sup>110</sup> Table 7.2: Caption . . . . .	72
<sup>111</sup> Table 7.3: Caption . . . . .	73

# <sup>112</sup> List of Figures

<sup>113</sup> Figure 2.1: Caption . . . . .	4
<sup>114</sup> Figure 2.2: Caption . . . . .	18
<sup>115</sup> Figure 2.3: Caption . . . . .	19
<sup>116</sup> Figure 2.4: Caption . . . . .	20
<sup>117</sup> Figure 3.1: Caption . . . . .	22
<sup>118</sup> Figure 3.2: Caption . . . . .	23
<sup>119</sup> Figure 5.1: . . . . .	35
<sup>120</sup> Figure 5.2: Caption . . . . .	40
<sup>121</sup> Figure 5.3: Caption . . . . .	42
<sup>122</sup> Figure 5.4: Caption . . . . .	45

<sup>123</sup>

## KEY TO ABBREVIATIONS

<sup>124</sup>

### Physical & mathematical quantities

<sup>125</sup>  $\chi^2$  chi-squared

<sup>126</sup>  $\Delta R$  angular distance

<sup>127</sup>  $\eta$  pseudorapidity

<sup>128</sup>  $E_T$  transverse energy

<sup>129</sup>  $E_T^{\text{miss}}$  missing transverse momentum

<sup>130</sup>  $\gamma_\mu$  Dirac matrices

<sup>131</sup>  $I$  weak isospin

<sup>132</sup>  $L$  instantaneous luminosity

<sup>133</sup>  $\mu$  signal strength

<sup>134</sup>  $p_T$  transverse momentum

<sup>135</sup>

### Particles

<sup>136</sup>  $b$  bottom quark

<sup>137</sup>  $pp$  proton-proton

<sup>138</sup>  $t\bar{t}$  top/anti-top quark

<sup>139</sup>  $t\bar{t}t\bar{t}$  four-top-quark

<sup>140</sup>  $tW$  single-top

<sup>141</sup>

### Acronyms

<sup>142</sup> **1LOS** one lepton, or two leptons of opposite charges

<sup>143</sup> **2HDM** two-Higgs doublet model

<sup>144</sup> **ATLAS** A Toroidal LHC ApparatuS

<sup>145</sup> **BDT** boosted decision tree

<sup>146</sup> **BSM** Beyond the Standard Model

<sup>147</sup> **CERN** European Organization for Nuclear Research

- <sub>148</sub> **CMS** Compact Muon Solenoid  
<sub>149</sub> **CR** control region  
<sub>150</sub> **ECIDS** Electron Charge ID Selector  
<sub>151</sub> **EM** electromagnetic  
<sub>152</sub> **EW** electroweak  
<sub>153</sub> **GNN** graph neural network  
<sub>154</sub> **GUT** Grand Unified Theory  
<sub>155</sub> **HLT** High-Level Trigger  
<sub>156</sub> **ID** inner detector  
<sub>157</sub> **JER** jet energy resolution  
<sub>158</sub> **JES** jet energy scale  
<sub>159</sub> **JVT** Jet Vertex Tagger  
<sub>160</sub> **L1** Level 1  
<sub>161</sub> **LH** likelihood  
<sub>162</sub> **LLH** log-likelihood  
<sub>163</sub> **LO** leading order  
<sub>164</sub> **LAr** liquid argon  
<sub>165</sub> **LHC** Large Hadron Collider  
<sub>166</sub> **MET** missing transverse energy  
<sub>167</sub> **NF** normalization factor  
<sub>168</sub> **NLO** next-to-leading order  
<sub>169</sub> **NNLO** next-to-next-to-leading order  
<sub>170</sub> **NP** nuisance parameter  
<sub>171</sub> **OP** operating point  
<sub>172</sub> **PS** parton shower  
<sub>173</sub> **PDF** parton distribution function  
<sub>174</sub> **PCBT** pseudo-continuous  $b$ -tagging

- <sub>175</sub> **QED** quantum electrodynamics
- <sub>176</sub> **QCD** quantum chromodynamics
- <sub>177</sub> **QFT** quantum field theory
- <sub>178</sub> **QmisID** charge mis-identification
- <sub>179</sub> **SF** scale factor
- <sub>180</sub> **SM** Standard Model
- <sub>181</sub> **SR** signal region
- <sub>182</sub> **SSML** two leptons of the same charge, or more than two leptons (multilepton)
- <sub>183</sub> **TDAQ** Trigger and Data Acquisition
- <sub>184</sub> **VEV** vacuum expectation value

<sup>185</sup> **Roadmap**

<sup>186</sup>	1. Finish adding bullets for all sections .....	06/04
<sup>187</sup>	Remaining	
<sup>188</sup>	• introduction	
<sup>189</sup>	2. Fill in details .....	06/13
<sup>190</sup>	• Add missing figures	
<sup>191</sup>	• Add missing bib	
<sup>192</sup>	3. Finalize analysis	
<sup>193</sup>	4. String everything together	
<sup>194</sup>	5. Miscellaneous/logistics (proofreading, review, ATLAS approval, etc.) .....	
<sup>195</sup>	6. Submission to the graduate school .....	07/01
<sup>196</sup>	7. Defense .....	07/15

<sub>197</sub> **Chapter 1. Introduction**

<sub>198</sub> 1. background and context

<sub>199</sub> 2. problem to be solved in thesis

<sub>200</sub> 3. aim of analysis:  $Z'$  consequences of many BSM theories, searching for  $Z'$

<sub>201</sub> 4. hypothesis/research question: searching for  $Z'$  in  $t\bar{t}t\bar{t}$  SSML channel

<sub>202</sub> 5. methodology: data collection - $\zeta$ , analysis regions - $\zeta$ , binned likelihood fit

<sub>203</sub> 6. thesis structure:

<sub>204</sub> • ch2: SM/BSM theoretical background

<sub>205</sub> • ch3: LHC/ATLAS experiment

<sub>206</sub> • ch4: samples used in the analysis

<sub>207</sub> • ch5: ATLAS particle reconstruction and identification techniques, and object  
<sub>208</sub> definitions for the analysis

<sub>209</sub> • ch6: analysis strategy

<sub>210</sub> • ch7: systematic uncertainties affecting the analysis

<sub>211</sub> • ch8: final results

<sub>212</sub> • ch9: summary

# <sup>213</sup> Chapter 2. Theoretical Overview

## <sup>214</sup> 2.1 The Standard Model

- <sup>215</sup> The Standard Model of physics (SM) is currently the most successful formalism to describe
- <sup>216</sup> the physical world at a microscopic scale.
- <sup>217</sup> The SM provides descriptions for all currently known elementary particles and three out of
- <sup>218</sup> four fundamental forces with the exception of gravity.

<sup>219</sup>

### <sup>220</sup> 2.1.1 Elementary particles

- <sup>221</sup> Elementary particles in the SM can be classified into two groups: bosons, consisting of particles following Bose-Einstein statistics with integer spin and fermions, consisting of particles following Fermi-Dirac statistics with half-integer spin
- <sup>224</sup> Fermions are the building blocks of composite particles and consequently all known matter, and can be further split into quarks & leptons.
- <sup>226</sup> Bosons act as force mediators for all fundamental forces described by the SM. Bosons have
- <sup>227</sup> two types: a scalar boson with spin 0 and vector gauge bosons with spin 1.
- <sup>228</sup> For each elementary particle there also exists a corresponding antiparticle with identical
- <sup>229</sup> mass and opposite charge (electric or color).

#### <sup>230</sup> Fermions

- <sup>231</sup> Quarks and leptons each has six flavors, grouped into three generations of doublets.
- <sup>232</sup> The six quark flavors consist of up ( $u$ ), down ( $d$ ), charm ( $c$ ), strange ( $s$ ), bottom ( $b$ ) and top

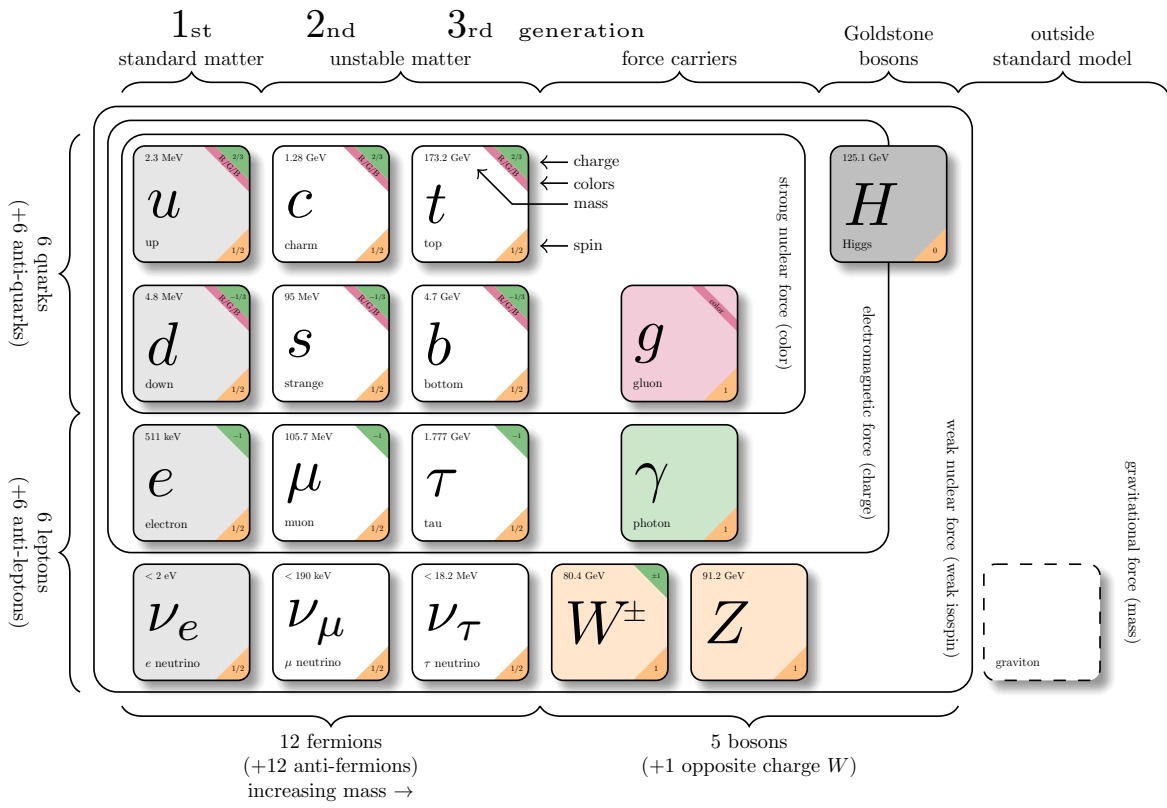


Figure 2.1: Caption[1]

<sup>233</sup> (t) quark flavors in increasing order of mass, forming three doublets ( $u, d$ ), ( $c, s$ ) and ( $t, b$ ).  
<sup>234</sup> Each doublet consists of one quark with electric charge of  $+2/3$  ( $u, s, t$ ), and one with charge  
<sup>235</sup> of  $-1/3$  ( $d, c, b$ ).  
<sup>236</sup> Each quark also has a property known as color charge, with possible values of red ( $R$ ), green  
<sup>237</sup> ( $G$ ), blue ( $B$ ) or antired ( $\bar{R}$ ), antigreen ( $\bar{G}$ ), and antiblue ( $\bar{B}$ ). Color charge follows color  
<sup>238</sup> confinement rules, which allows only configurations of quarks with neutral color charge to  
<sup>239</sup> exist in isolation. Neutral charge configurations can be formed from either a set of three  
<sup>240</sup> colors ( $R, G, B$ ), a set of a color and its anticolor ( $q, \bar{q}$ ), or any combination of the two.  
<sup>241</sup> Consequently, no isolated quark can exist in a vacuum and can only exist in bound states  
<sup>242</sup> called hadrons.  
<sup>243</sup> Quarks are the only elementary particles in the SM that can interact with all four funda-  
<sup>244</sup> mental forces.  
<sup>245</sup> The three leptons doublets consist of electron ( $e$ ), muon ( $\mu$ ), tau ( $\tau$ ) and their respective  
<sup>246</sup> neutrino flavors: electron neutrino ( $\nu_e$ ), muon neutrino ( $\nu_\mu$ ) and tau neutrino ( $\nu_\tau$ )  
<sup>247</sup> Charged leptons ( $e, \mu, \tau$ ) carry an electric charge of  $-1$ , while their antiparticles carry the  
<sup>248</sup> opposite charge  $+1$  and their corresponding neutrino flavors carrying no charge (charge neu-  
<sup>249</sup> tral).  
<sup>250</sup> Charged leptons interact with all fundamental forces except the strong force, while neutrinos  
<sup>251</sup> only interact with the weak force and gravity.

## <sup>252</sup> **Bosons**

<sup>253</sup> The SM classify bosons into two types: one scalar boson with spin 0 known as the Higgs  
<sup>254</sup> ( $H$ ) boson, and vector gauge bosons with spin 1 known as gluons ( $g$ ), photon ( $\gamma$ ),  $W^\pm$  and  
<sup>255</sup>  $Z$  bosons.

- <sup>256</sup> The gluons and photon are massless, while the  $W^\pm$ ,  $Z$  and  $H$  are massive.
- <sup>257</sup> Each vector gauge boson serves as the mediator for a fundamental force described by the
- <sup>258</sup> SM.
- <sup>259</sup> Gluons are massless mediator particles for the strong interaction between quarks according
- <sup>260</sup> to quantum chromodynamics (QCD), and carry the color charge in a strong interaction.
- <sup>261</sup> Each gluon carries a non-neutral color charge out of eight linearly independent color states
- <sup>262</sup> in the gluon color octet.
- <sup>263</sup> Photon is the massless and charge-neutral mediator particle for the electromagnetic interac-
- <sup>264</sup> tion following quantum electrodynamics (QED).
- <sup>265</sup> The  $W^\pm$  and  $Z$  bosons are massive mediator particles for the weak interaction, with the
- <sup>266</sup>  $W^\pm$  boson carrying an electric charge of  $\pm 1$  while the  $Z$  boson is charge neutral.
- <sup>267</sup> Other than the vector gauge boson, the only scalar boson in the SM is the Higgs boson which
- <sup>268</sup> is massive with electric charge of 0.
- <sup>269</sup> The Higgs boson does not mediate a fundamental force like vector bosons, but serve to
- <sup>270</sup> provide the rest mass for all massive elementary particles in the SM through the Higgs
- <sup>271</sup> mechanism.

### <sup>272</sup> 2.1.2 Mathematical formalism

- <sup>273</sup> The SM can be described within the formalism of quantum field theory (QFT) with the
- <sup>274</sup> Lagrangian

$$\mathcal{L}_{\text{SM}} = \mathcal{L}_{\text{QCD}} + \underbrace{(\mathcal{L}_{\text{gauge}} + \mathcal{L}_{\text{fermion}} + \mathcal{L}_{\text{Higgs}} + \mathcal{L}_{\text{Yukawa}})}_{\mathcal{L}_{\text{EW}}} \quad (2.1)$$

- <sup>275</sup> where  $\mathcal{L}_{\text{QCD}}$  is the QCD term and  $\mathcal{L}_{\text{EW}}$  is the electroweak (EW) term of the Lagrangian.
- <sup>276</sup> QFT treats particles as excitations of their corresponding quantum fields: fermion field  $\psi$ ,

277 electroweak boson fields  $W_{1,2,3}$  &  $B$ , gluon field  $G_\alpha$  and Higgs field  $\phi$ .

278 QFT depends heavily on gauge theory. A quantum field has gauge symmetry if there exists  
279 a continuous gauge transformation that when applied to every point (local gauge transfor-  
280 mation) leaves the field Lagrangian unchanged. The set of gauge transformations of a gauge  
281 symmetry is the symmetry group of the field, which comes with a set of generators, each with  
282 a corresponding gauge field. Under QFT, the quanta of these gauge fields are called gauge  
283 bosons. The SM Lagrangian is gauge invariant under global Poincaré symmetry and local  
284  $SU(3)_C \times SU(2)_L \times U(1)_Y$  gauge symmetry, with the gauge term  $SU(3)_C$  corresponding to  
285 the strong interaction and  $SU(2)_L \times U(1)_Y$  to the EW interaction.

286 Global Poincaré symmetry ensures that  $\mathcal{L}_{\text{SM}}$  satisfies translational symmetry, rotational  
287 symmetry and Lorentz boost frame invariance. By Noether's theorem, gauge symmetries  
288 lead to corresponding conservation laws which leads to conservation of momentum, angular  
289 momentum and energy in the SM.

## 290 Quantum chromodynamics

291 QCD is a non-Abelian gauge theory (Yang-Mills theory) describing the strong interaction  
292 between quarks in the SM with the gauge group  $SU(3)_C$ , where  $C$  represents conservation  
293 of color charge under  $SU(3)_C$  symmetry.

294 According to QFT, quarks can be treated as excitations of corresponding quark fields  $\psi$ .  
295 Quark fields are invariant under  $SU(3)_C$  transformation

$$\psi \rightarrow e^{i\theta(x)T_a}\psi \quad (2.2)$$

<sup>296</sup> where  $T_a$  are generators of  $SU(3)_C$ , represented as  $T_a = \lambda_a/2$  with  $\lambda_a$  being the eight Gell-Mann matrices.

<sup>298</sup> The free Dirac Lagrangian

$$\mathcal{L}_0 = \bar{\psi}(i\gamma^\mu \partial_\mu - m)\psi \quad (2.3)$$

<sup>299</sup> is invariant under global  $SU(3)$  symmetry, but not under local  $SU(3)_C$  symmetry. To <sup>300</sup> establish invariance under local  $SU(3)_C$  symmetry, the gauge covariant derivative  $D_\mu$  is <sup>301</sup> defined so that

$$D_\mu \psi = (\partial_\mu - ig_s G_\mu^a T_a) \psi, \quad (2.4)$$

<sup>302</sup> where  $g_s = \sqrt{4\pi\alpha_s}$  is the QCD coupling constant,  $G_\mu^a(x)$  are the eight gluon fields that <sup>303</sup> transform under  $SU(3)_C$  as

$$G_\mu^a \rightarrow e^{iT_a \theta_a(x)} \left( G_\mu^a + \frac{i}{g_s} \partial_\mu \right) e^{-iT_a \theta_a(x)} = G_\mu^a - \frac{1}{g_s} \partial_\mu \theta_a(x) - f_{abc} \theta_b(x) G_\mu^c, \quad (2.5)$$

<sup>304</sup> and  $T_a$  are the generators of  $SU(3)_C$  defined as  $T_a = \lambda_a/2$  with  $\lambda_a$  being the eight Gell-Mann <sup>305</sup> matrices.

<sup>306</sup> Defining the gluon field strength tensor  $G_{\mu\nu}^a$  as

$$G_{\mu\nu}^a \equiv \partial_\mu G_\nu^a - \partial_\nu G_\mu^a - g_s f^{abc} G_\mu^b G_\nu^c, \quad (2.6)$$

<sup>307</sup> where  $f^{abc}$  are the structure constants of  $SU(3)_C$ , the gauge invariant QCD Lagrangian is

$$\mathcal{L}_{\text{QCD}} = \bar{\psi}(i\gamma^\mu D_\mu - m)\psi - \frac{1}{4} G_{\mu\nu}^a G_a^{\mu\nu}, \quad (2.7)$$

<sup>308</sup> which can be expressed in the form of

$$\mathcal{L}_{\text{QCD}} = \underbrace{-\frac{1}{4}G_{\mu\nu}^a G_a^{\mu\nu}}_{\text{gluon kinematics}} + \underbrace{\bar{\psi}(i\gamma^\mu \partial_\mu - m)\psi}_{\text{quark kinematics}} + \underbrace{\bar{\psi}^i(g_s \gamma^\mu (T_a)_{ij} G_\mu^a) \bar{\psi}^j}_{\text{quark-gluon interaction}}. \quad (2.8)$$

<sup>309</sup> with  $i, j$  being the color indices with integer values from 1 to 3. The noncommutativity  
<sup>310</sup> of  $SU(3)_C$  gives rise to an additional term consisting of only gluon fields and gluon-gluon  
<sup>311</sup> interactions. Additionally, the Lagrangian also forces gluons to be massless to maintain  
<sup>312</sup> gauge invariance.

### <sup>313</sup> Electroweak theory

<sup>314</sup> The electroweak interaction is the unified description of the weak interaction and electro-  
<sup>315</sup> magnetism under the  $SU(2)_L \times U(1)_Y$  symmetry group, where  $L$  represents the left-handed  
<sup>316</sup> chirality of the weak interaction and  $Y$  represents the weak hypercharge quantum number.

<sup>317</sup> The quantum number associated with the weak chirality is the weak isospin  $I$ . The EW  
<sup>318</sup> quantum numbers are connected by the Gell-Mann-Nishijima relation

$$Q = I_3 + Y/2 \quad (2.9)$$

<sup>319</sup> where  $Q$  is the electric charge and  $I_3$  is the third component of weak isospin  $I$ .

<sup>320</sup> Fermions can have either left-handed or right-handed chirality, and can be divided into  
<sup>321</sup> left-handed doublets and right-handed singlets

$$\psi_L = \begin{pmatrix} \nu_e \\ e_L \end{pmatrix}, \begin{pmatrix} \nu_\mu \\ \mu_L \end{pmatrix}, \begin{pmatrix} \nu_\tau \\ \tau_L \end{pmatrix}, \begin{pmatrix} u_L \\ d_L \end{pmatrix}, \begin{pmatrix} c_L \\ s_L \end{pmatrix}, \begin{pmatrix} t_L \\ b_L \end{pmatrix} \quad (2.10)$$

$$\psi_R = e_R, \mu_R, \tau_R, u_R, d_R, c_R, s_R, t_R, b_R,$$

- <sup>322</sup> with the exception of neutrino which can only have left-handed chirality in the SM.  
<sup>323</sup> Both left-handed and right-handed fermion fields are invariant under  $U(1)_Y$  transformation

$$\psi \rightarrow e^{iY\theta(x)/2}\psi. \quad (2.11)$$

- <sup>324</sup> Similar to QCD, to establish invariance under local  $U(1)_Y$  symmetry, the  $U(1)_Y$  gauge  
<sup>325</sup> covariant derivative  $D_\mu$  is defined as

$$D_\mu\phi = \left(\partial_\mu - ig'\frac{Y}{2}B_\mu\right)\psi \quad (2.12)$$

- <sup>326</sup> where  $B_\mu(x)$  is a vector gauge field that transforms under  $U(1)_Y$  as

$$B_\mu \rightarrow B_\mu + \frac{1}{g'}\partial_\mu\theta(x) \quad (2.13)$$

- <sup>327</sup> and  $g'$  is the  $B_\mu$  coupling constant.

- <sup>328</sup> Right-handed fermion singlets are not affected by  $SU(2)_L$  transformation, so fermion fields  
<sup>329</sup> transform under  $SU(2)_L$  as

$$\begin{aligned} \psi_L &\rightarrow e^{iI_3\vec{\theta}(x)\cdot\vec{\sigma}/2}\psi_L \\ \psi_R &\rightarrow \psi_R. \end{aligned} \quad (2.14)$$

- <sup>330</sup> where  $\vec{\sigma}/2$  are generators of  $SU(2)_L$  and  $\vec{\sigma}$  are Pauli matrices. In order to preserve local  
<sup>331</sup> symmetry, the gauge covariant derivative for  $SU(2)_L$  is defined as

$$D_\mu\psi_L = \left(\partial_\mu - ig\frac{\sigma_i}{2}W_\mu^i\right)\psi_L \quad (2.15)$$

<sup>332</sup> where  $W_\mu^i(x)$  ( $i = 1, 2, 3$ ) are three boson gauge fields that transform under  $SU(2)_L$  as

$$W_\mu^i \rightarrow e^{i\frac{\sigma_i}{2}\theta_i(x)} \left( W_\mu^i + \frac{i}{g}\partial_\mu \right) e^{-i\frac{\sigma_i}{2}\theta_i(x)} = W_\mu^i + \frac{2}{g}\partial_\mu\theta_a(x) + \epsilon^{ijk}\theta_j(x)W_\mu^k, \quad (2.16)$$

<sup>333</sup> with  $g$  as the gauge coupling constant for  $W_\mu^i$ , and  $\epsilon^{ijk}$  as the structure constant for  $SU(2)_L$ .

<sup>334</sup> The gauge covariant derivative for  $SU(2)_L \times U(1)_Y$  can then be written as

$$\begin{aligned} D_\mu\psi_L &= \left( \partial_\mu - ig'\frac{Y_L}{2}B_\mu - ig\frac{\sigma_i}{2}W_\mu^i \right) \psi_L \\ D_\mu\psi_R &= \left( \partial_\mu - ig'\frac{Y_R}{2}B_\mu \right) \psi_R. \end{aligned} \quad (2.17)$$

<sup>335</sup> Similar to QCD, the kinetic term is added by defining field strengths for the four gauge fields

$$\begin{aligned} B_{\mu\nu} &\equiv \partial_\mu B_\nu - \partial_\nu B_\mu \\ W_{\mu\nu}^i &\equiv \partial_\mu W_\nu^i - \partial_\nu W_\mu^i - ge^{ijk}W_\mu^jW_\nu^k. \end{aligned} \quad (2.18)$$

<sup>336</sup> The local  $SU(2)_L \times U(1)_Y$  invariant EW Lagrangian can then be expressed as

$$\begin{aligned} \mathcal{L}_{\text{EW}} &= i\bar{\psi}(\gamma^\mu D_\mu)\psi - \frac{1}{4}W_{\mu\nu}^iW_i^{\mu\nu} - \frac{1}{4}B_{\mu\nu}B^{\mu\nu} \\ &= \underbrace{i\bar{\psi}(\gamma^\mu\partial_\mu)\psi}_{\text{fermion kinematics}} - \underbrace{\bar{\psi}\left(\gamma^\mu g'\frac{Y}{2}B_\mu\right)\psi}_{\text{fermion-gauge boson interaction}} - \underbrace{\bar{\psi}_L\left(\gamma^\mu g\frac{\sigma_i}{2}W_\mu^i\right)\psi_L}_{\text{boson kinematics \& self-interaction}} - \frac{1}{4}W_{\mu\nu}^iW_i^{\mu\nu} - \frac{1}{4}B_{\mu\nu}B^{\mu\nu}. \end{aligned} \quad (2.19)$$

<sup>337</sup> The EW  $Z$ ,  $\gamma$  and  $W^\pm$  bosons can be extracted from  $\mathcal{L}_{\text{EW}}$  by reparameterizing the weak  
<sup>338</sup> hypercharge gauge boson  $B_\mu$  and weak isospin gauge bosons  $W_\mu^i$  as

$$W^\pm \equiv \frac{1}{\sqrt{2}} (W_\mu^1 \mp i W_\mu^2)$$

$$\begin{pmatrix} A \\ Z^0 \end{pmatrix} \equiv \begin{pmatrix} \cos \theta_W & \sin \theta_W \\ -\sin \theta_W & \cos \theta_W \end{pmatrix} \begin{pmatrix} B_\mu \\ W_\mu^3 \end{pmatrix} \quad (2.20)$$

<sup>339</sup> where  $\theta_W \equiv \cos^{-1} \left( g / \sqrt{g^2 + g'^2} \right)$  is the weak mixing angle. The boson kinetic term can also  
<sup>340</sup> be refactorized to extract cubic (three vertices) and quartic (four vertices) self-interactions  
<sup>341</sup> among the gauge bosons [2].

<sup>342</sup> The EW Lagrangian can then be rewritten as

$$\mathcal{L}_{\text{EW}} = \underbrace{e A_\mu \bar{\psi} (\gamma^\mu Q) \psi}_{\text{electromagnetism}} + \underbrace{\frac{e}{2 \sin \theta_W \cos \theta_W} \bar{\psi} \gamma^\mu (v_f - a_f \gamma_5) \psi Z_\mu}_{\text{neutral current interaction}}$$

$$+ \underbrace{\frac{g}{2\sqrt{2}} \sum_{\psi_L} [\bar{f}_2 \gamma^\mu (1 - \gamma_5) f_1 W_\mu^+ + \bar{f}_1 \gamma^\mu (1 - \gamma_5) f_2 W_\mu^-]}_{\text{charged current interaction}} \quad (2.21)$$

$$+ \mathcal{L}_{\text{kinetic}} + \underbrace{\mathcal{L}_{\text{cubic}} + \mathcal{L}_{\text{quartic}}}_{\text{boson self-interaction}}$$

<sup>343</sup> where  $a_f = I_3$ ,  $v_f = I_3(1 - 4|Q| \sin^2 \theta_W)$  and  $f_1$ ,  $f_2$  are up and down type fermions of a  
<sup>344</sup> left-handed doublet.

## <sup>345</sup> Higgs mechanism

<sup>346</sup> So far, the  $EW$  bosons are massless according to the  $EW$  Lagrangian, since the mass terms  
<sup>347</sup>  $-m\bar{\psi}\psi$  for fermions and  $-mA^\mu A_\mu$  for bosons are not invariant under the  $EW$  Lagrangian.

348 The particles must then acquire mass under another mechanism. The Brout-Engler-Higgs  
349 mechanism [3–5] was introduced in 1964 to rectify this issue, and verified in 2012 with the  
350 discovery of the Higgs boson [6, 7].  
351 The Higgs potential is expressed as

$$V(\phi^\dagger \phi) = \mu^2 \phi^\dagger \phi + \lambda (\phi^\dagger \phi)^2 \quad (2.22)$$

352 where  $\mu^2$  and  $\lambda > 0$  are arbitrary parameters, and the  $SU(2)_L$  doublet  $\phi$  is the Higgs field

$$\phi = \begin{pmatrix} \phi^+ \\ \phi^0 \end{pmatrix}, \quad (2.23)$$

353 with complex scalar fields  $\phi^+$  and  $\phi^0$  carrying +1 and 0 electric charge respectively. The  
354 Lagrangian for a scalar field is

$$\mathcal{L}_H = (\partial_\mu \phi)^\dagger (\partial^\mu \phi) - V(\phi^\dagger \phi). \quad (2.24)$$

355 Since the potential  $V(\phi)$  is constrained by  $\lambda > 0$ , the ground state is solely controlled by  $\mu$ .  
356 If  $\mu^2 > 0$ , the ground state would be  $\phi = 0$ , and the EW bosons would remain massless. If  
357  $\mu^2 < 0$ , the ground state would be

$$|\phi|^2 = -\frac{\mu^2}{2\lambda} \equiv \frac{v^2}{\sqrt{2}}, \quad (2.25)$$

358 where  $v$  is defined as the vacuum expectation value (VEV). The standard ground state for  
359 the Higgs potential without loss of generality can be chosen as

$$\phi(0) = \frac{1}{\sqrt{2}} \begin{pmatrix} 0 \\ v \end{pmatrix}. \quad (2.26)$$

### sombrero potential pic

Due to  $U(1)$  invariance, any  $-e^{i\theta}\sqrt{\mu^2/\lambda}$  is a ground state for the Higgs Lagrangian. This vacuum state degeneracy results in spontaneous symmetry breaking of the  $SU(2)_L \times U(1)_Y$  symmetry into  $U(1)_{\text{EM}}$  symmetry. The spontaneous symmetry breaking introduces three massless (Nambu-Goldstone) vector gauge boson  $\xi$  and a massive scalar boson  $\eta$ , each corresponds to a generator of the gauge group. The bosons can be extracted using the reparameterization [8]

$$\xi \equiv \phi^+ \sqrt{2}, \quad \eta \equiv \phi^0 \sqrt{2} - v, \quad (2.27)$$

360 such that  $\xi, \eta$  are real fields. The Higgs field now become

$$\phi = \frac{v + \eta + i\xi}{\sqrt{2}} = e^{i\xi \cdot \frac{\sigma}{2v}} \begin{pmatrix} 0 \\ \frac{v + \eta}{\sqrt{2}} \end{pmatrix}. \quad (2.28)$$

361 Due to  $U(1)_{\text{EM}}$  invariance, a unitary gauge with the transformation  $\phi \rightarrow \exp(-i\xi \cdot \frac{\sigma}{2v})$  can  
362 be chosen to eliminate the massless bosons, leaving the massive  $\eta$  which can now be observed  
363 as an excitation of the Higgs field  $\phi$  and consequently the Higgs boson  $h$ . Using the EW  
364 covariant derivative from Equation 2.17, the Higgs Lagrangian around the vacuum state

<sup>365</sup> becomes

$$\begin{aligned}\mathcal{L}_H &= (D_\mu \phi)^\dagger (D^\mu \phi) - \mu^2 \left( \frac{v+h}{\sqrt{2}} \right)^2 - \lambda \left( \frac{v+h}{\sqrt{2}} \right)^4 \\ &= (D_\mu \phi)^\dagger (D^\mu \phi) - \frac{1}{2} \mu^2 h^2 - \lambda v h^3 - \frac{\lambda}{4} h^4 - \dots\end{aligned}\tag{2.29}$$

<sup>366</sup> The Higgs mass can be extracted from the quadratic term as  $m_H = \sqrt{-2\mu^2}$ . The kinetic  
<sup>367</sup> term in the Lagrangian can be written as

$$\begin{aligned}(D_\mu \phi)^\dagger (D^\mu \phi) &= \frac{1}{2} (\partial_\mu h)^2 + \frac{g^2}{8} (v+h)^2 \left| W_\mu^1 - i W_\mu^2 \right|^2 + \frac{1}{8} (v+h)^2 (g' W_\mu - g B_\mu) \\ &= \frac{1}{2} (\partial_\mu h)^2 + (v+h)^2 \left( \frac{g^2}{4} W_\mu^+ W^{-,\mu} + \frac{1}{8} (g^2 + g'^2) Z_\mu^0 Z^{0,\mu} \right),\end{aligned}\tag{2.30}$$

<sup>368</sup> using the reparameterization from Equation 2.20. Masses for the EW bosons can be extracted  
<sup>369</sup> from the quadratic terms

$$m_{W^\pm} = \frac{v}{2} g, \quad m_Z = \frac{v}{2} \sqrt{g^2 + g'^2}, \quad m_\gamma = 0.\tag{2.31}$$

<sup>370</sup> Fermions acquire mass via Yukawa interactions with the scalar Higgs field [8], which add a  
<sup>371</sup> term to the Lagrangian

$$\begin{aligned}\mathcal{L}_{\text{Yukawa}} &= -c_f \frac{v+h}{\sqrt{2}} (\bar{\psi}_R \psi_L + \bar{\psi}_L \psi_R) \\ &= -\underbrace{\frac{c_f}{\sqrt{2}} v (\bar{\psi} \psi)}_{\text{fermion mass}} - \underbrace{\frac{c_f}{\sqrt{2}} (h \bar{\psi} \psi)}_{\text{fermion-Higgs interaction}},\end{aligned}\tag{2.32}$$

<sup>372</sup> where  $c_f$  is the fermion-Higgs Yukawa coupling. The fermion mass is then  $m_f = c_f v / \sqrt{2}$ .

<sup>373</sup> **2.1.3 Shortcomings of the Standard Model**

<sup>374</sup> **Gravity and general relativity**

<sup>375</sup> **Grand Unified Theory (GUT**

<sup>376</sup> **Dark energy and dark matter**

<sup>377</sup> **Hierarchy problem**

<sup>378</sup> **Matter-antimatter asymmetry**

<sup>379</sup> **Neutrino masses**

<sup>380</sup> **2.2 Beyond the Standard Model**

<sup>381</sup> **2.2.1 Top-philic vector resonance**

<sup>382</sup> Many BSM models extend the SM by adding to the EW gauge group additional  $U(1)'$

<sup>383</sup> gauge symmetries, each with an associated vector gauge boson nominally named  $Z'$  [9].

<sup>384</sup> In the case of a BSM global symmetry group with rank larger than the SM gauge group,

<sup>385</sup> the symmetry group can break into  $G_{\text{SM}} \times U(1)'^n$ , where  $G_{\text{SM}}$  is the SM gauge group

<sup>386</sup>  $SU(3)_C \times SU(2)_L \times U(1)_Y$  and  $U(1)'^n$  is any  $n \geq 1$  number of  $U(1)'$  symmetries. The

<sup>387</sup> existence of additional vector bosons  $Z'$  would also open up many avenues of new physics

<sup>388</sup> e.g. extended Higgs sectors from  $U(1)'$  symmetry breaking, existence of flavor-changing

<sup>389</sup> neutral current (FCNC) effects in some models, and possible exotic production from heavy

<sup>390</sup>  $Z'$  decays [9]

<sup>391</sup> Due to the top quark having the largest mass out of all known elementary particles in the SM,

<sup>392</sup> many BSM models [10–13] predict ‘top-philic’ vector resonances that have much stronger

<sup>393</sup> coupling to the top quark compared to other quarks such that the coupling factors to lighter  
<sup>394</sup> quarks are negligible.

<sup>395</sup> The analysis in this thesis attempts to reconstruct the resonance directly to avoid dependency  
<sup>396</sup> on model choice. In addition, a simplified color-singlet vector particle model [14, 15] is  
<sup>397</sup> employed to study model-dependent interpretations. The interaction Lagrangian assumes  
<sup>398</sup> only coupling with the top quark, expressed as

$$\begin{aligned}\mathcal{L}_{Z'} &= \bar{t}\gamma_\mu(c_L P_L + c_R P_R) t Z'^\mu \\ &= c_t \bar{t}\gamma_\mu (\cos\theta P_L + \sin\theta P_R) t Z'^\mu\end{aligned}\tag{2.33}$$

<sup>399</sup> where  $c_t = \sqrt{c_L^2 + c_R^2}$  is the top coupling strength,  $P_{L/R} = (1 \mp \gamma_5)/2$  are the chirality  
<sup>400</sup> projection operators, and  $\theta = \tan^{-1}(c_R/c_L)$  is the chirality mixing angle [14].

<sup>401</sup> Assuming the  $Z'$  mass  $m_{Z'}$  is much larger than the top mass ( $m_t^2/m_{Z'}^2 \approx 0$ ), the  $Z'$  decay  
<sup>402</sup> width at leading-order (LO) can be approximated as

$$\Gamma(Z' \rightarrow t\bar{t}) \approx \frac{c_t^2 m_{Z'}}{8\pi}.\tag{2.34}$$

<sup>403</sup> The main production channels for the aforementioned heavy topophilic color singlet  $Z'$  are at  
<sup>404</sup> tree level and loop level, with the one-loop level being the dominant processes. To minimize  
<sup>405</sup> model dependence, only the tree level production was considered. The Feynman diagrams  
<sup>406</sup> for tree level production channels are shown in Figure 2.2, with  $pp \rightarrow Z' + t\bar{t} \rightarrow t\bar{t}t\bar{t}$  having  
<sup>407</sup> the largest contribution out of the three.

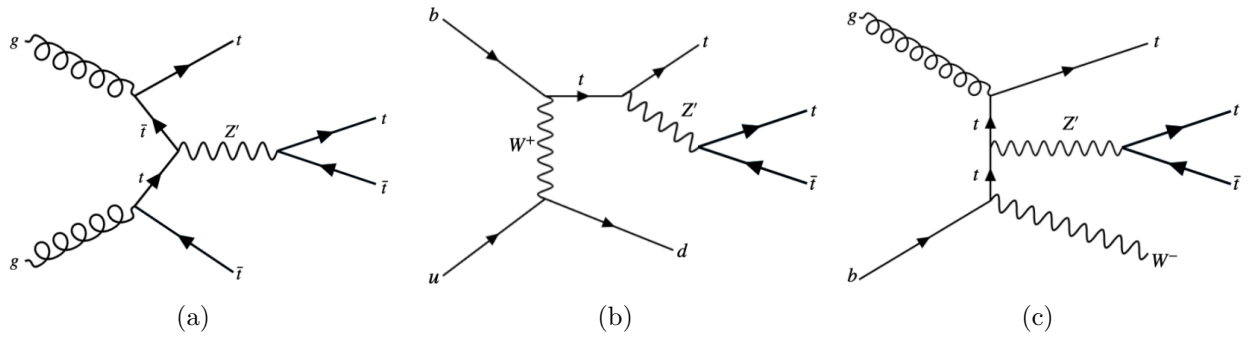


Figure 2.2: tree level  $Z'$  production in association with (a)  $t\bar{t}$  to 4tops, (b)  $tj$  (light quark) to 3tops, (c)  $tW$  to 3 tops, derived from top quark final states produced via strong, EW and mixed QCD-EW interactions [14]

## 408 2.3 Four-top quark production

409 As of now, the top quark is the heaviest particle in the SM with mass of about 173 GeV.

410 This also gives it the strongest coupling to the Higgs boson and new resonances in various

411 proposed BSM models ([citations](#)), making the top quark and its processes attractive vehicles

412 with which to probe BSM physics.

413 The analysis presented in this thesis uses the  $t\bar{t}t\bar{t}$  final state signal signature to search for

414 the existence of a heavy BSM resonance that couples strongly to the top quark.

415 Production of  $t\bar{t}t\bar{t}$  is a rare process predicted by the SM with a predicted cross section of

416  $\sigma_{t\bar{t}t\bar{t}} = 12 \pm 2.4$  fb at next-to-leading (NLO) in QCD including EW corrections. Including

417 threshold summation at NLO logarithmic accuracy raises total production cross section by

418  $\approx 12\%$  and significantly reduces scale uncertainty, which gives  $\sigma_{t\bar{t}t\bar{t}} = 13.4^{+1.0}_{-1.8}$  fb.

419 Typical tree level SM  $t\bar{t}t\bar{t}$  production processes are shown in Figure 2.3. Cross section for  $t\bar{t}t\bar{t}$

420 production can be enhanced by many possible BSM models, in particular possible production

421 of a heavy neutral resonance boson  $X$ , decaying to a  $t\bar{t}$  pair, in association with a  $t\bar{t}$  pair in

422 composite Higgs scenarios ([citations](#)) or two-Higgs-doublet-model (2HDM).

<sup>423</sup> The  $t\bar{t}X$  production mode and consequently  $t\bar{t}t\bar{t}$  signal signature can provide a more sensitive  
<sup>424</sup> channel for searches by avoiding contamination from the large  $gg \rightarrow t\bar{t}$  SM background in  
<sup>425</sup> an inclusive  $X \rightarrow t\bar{t}$  search.

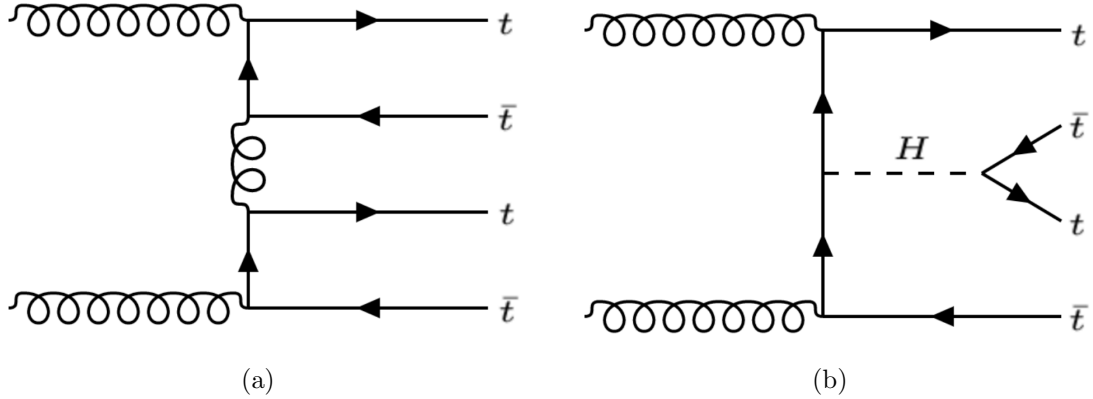


Figure 2.3: tree level, mediator particle in (b) can be gluon, neutral gauge boson ( $Z/\gamma$ ) or Higgs [16]

426 SM production of  $t\bar{t}t\bar{t}$  was observed by ATLAS in 2023 in the SSML channel using an  
 427 integrated luminosity of  $140 \text{ fb}^{-1}$  [16], with an observed (expected) significance level of  $6.1\sigma$   
 428 (4.3 $\sigma$ ) compared to the background-only hypothesis. The observed cross section is measured  
 429 to be  $\sigma_{t\bar{t}t\bar{t}} = 22.5^{+6.6}_{-5.5} \text{ fb}$ , consistent with SM prediction within 1.8 $\sigma$ .

431 Decay modes

<sup>432</sup> Due to its mass, the top quark has a very short lifetime of  $10^{-24}$ s, and consequently decays  
<sup>433</sup> before it can hadronize. The top quark decays to a  $W$  boson and a  $b$ -quark with a branching  
<sup>434</sup> ratio of almost 100%, and is assumed to be such for the purpose of this analysis. The  $W$  boson  
<sup>435</sup> can subsequently decay hadronically or leptonically, with branching ratios of approximately  
<sup>436</sup> 68% and 32% respectively, with all lepton flavors having similar ratios assuming lepton

437 universality. This results in many different final states for  $t\bar{t}t\bar{t}$  decay, which can each be  
438 classified into one of three channels: all hadronic decays; exactly one lepton or two opposite-  
439 sign leptons (1LOS); exactly two same-sign leptons or three or more leptons (SSML). The  
440 branching ratio for each channel is shown in Figure 2.4.

441 The all hadronic and 1LOS channels have much larger branching ratios compared to SSML  
442 channel but suffer heavily from irreducible  $gg \rightarrow t\bar{t}$  background contamination, giving SSML  
443 channel better sensitivity at the cost of lower statistics. This is also the targeted channel for  
444 the analysis in this thesis.

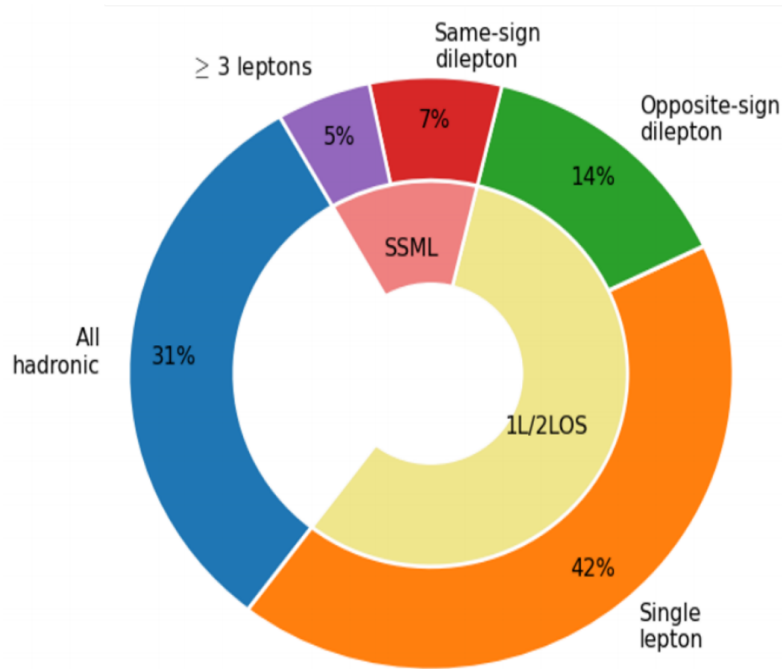


Figure 2.4: Caption

# 445 Chapter 3. LHC & ATLAS Experiment

## 446 3.1 The Large Hadron Collider

447 theoretical predictions are tested with experimental data obtained from particle accelerators  
448 world's largest accelerator built by CERN situated on the border of Switzerland and France  
449 has been operating since xxxx  
450 lifetime divided into 3 runs, currently on Run 3 with planned upgrades on the horizon  
451 responsible for a number of discoveries aka Higgs, etc.

### 452 3.1.1 Overview

453 [Basic info: location, size, main working mechanism, main detectors, main physics done]  
454 - 27 km circumference, reusing LEP tunnels 175 m below ground level  
455 - 7-13-13.6 TeV center of mass energies for pp collisions  
456 - other than pp, also collides pPb, PbPb at 4 points with 4 main detectors: ATLAS, CMS  
457 (general purpose detectors), ALICE (heavy ion physics, ion collisions), LHCb (*b*-physics)

### 458 3.1.2 LHC operations

459 - focuses mainly on pp collisions for this thesis - beams split into bunches of  $1.1 \times 10^{11}$   
460 protons with instantaneous luminosity of up to  $2 \times 10^{34} \text{ cm}^{-2}\text{s}^{-1}$   
461 - beam energies ramp up in other accelerators before injection, full ramp up to 6.5 GeV  
462 about 20 minutes  
463 (insert full diagram of accelerator chain)  
464 Linac 4: hydrogen atoms, accelerated up to 160 MeV

<sup>465</sup> PSB: H atoms stripped of electrons before injection, accelerated to 2 GeV

<sup>466</sup> PS: 26 GeV, SPS: 450 GeV

<sup>467</sup> LHC: injection in opposite directions, 6.5 TeV per beam

<sup>468</sup>

<sup>469</sup> Run 1: 2010-2012, Run 2: 2015-2018, Run 3: 2022-2025, HL-LHC: 2029-?

<sup>470</sup> COM energies: 7 & 8 TeV, 13 TeV, 13.6 TeV, 13.6 & 14 TeV

<sup>471</sup>

<sup>472</sup> inbetween periods: long shutdowns (LS1, LS2, LS3)

<sup>473</sup>



Figure 3.1: Caption [17]

474 Physics at the LHC

475 history (CDF/D0)

476 LHC as a top factory: show luminosity and cross section for top processes

477 couples to Higgs as heaviest elementary particle

478 Higgs produced mainly from ggH (90%) via top loop and from ttH

479

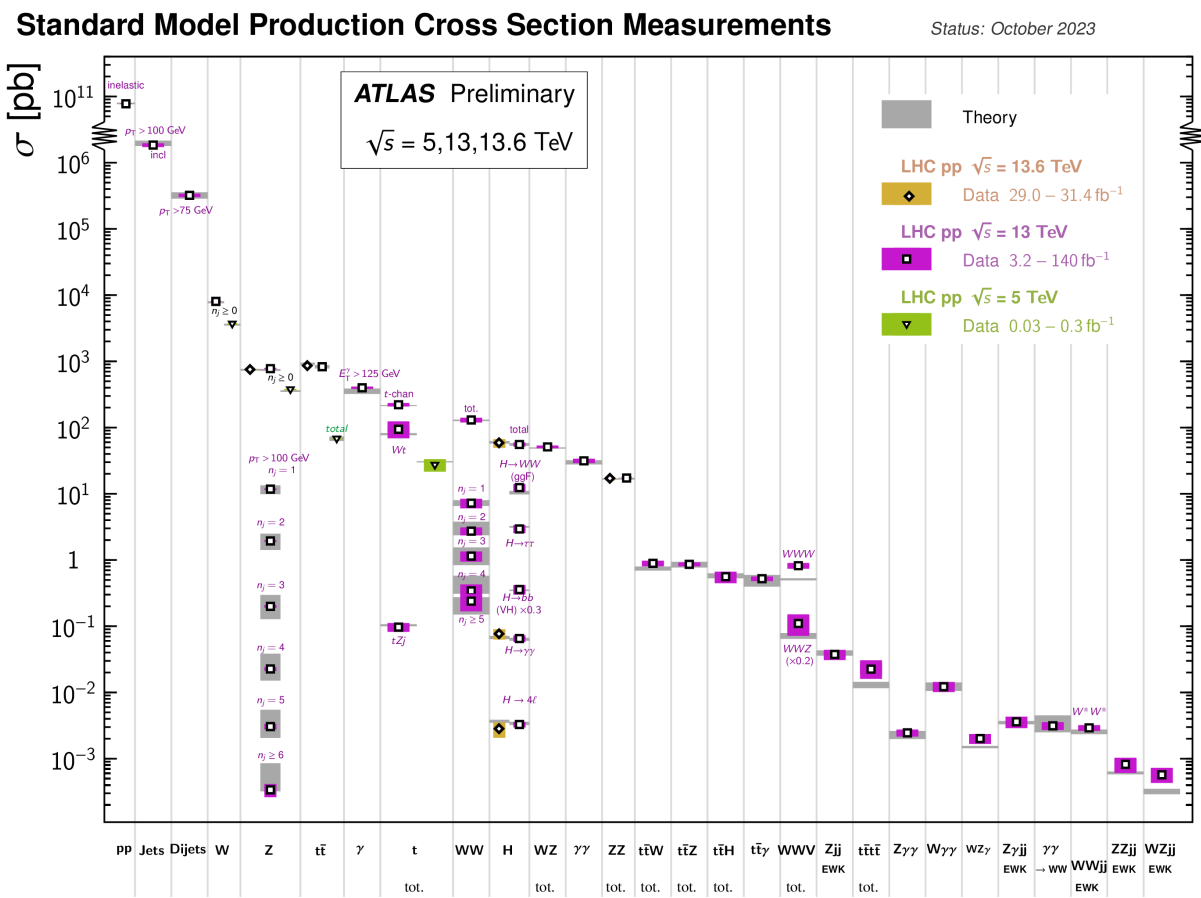


Figure 3.2: Caption [18]

## 480 3.2 The ATLAS detector

481 multipurpose particle detector with a symmetric cylindrical geometry and a solid angle

482 coverage of almost  $4\pi$

483 44m long, 25m diameter

484 inner detector, solenoid/toroid magnet, EM & hadronic calorimeters, muon spectrometer

485 (insert figure)

486 right-handed cylindrical system, z-axis follows beamline, azimuthal and polar (0 in the  
487 beam direction) angles measured with respect to beam axis.

488 pseudorapidity  $\eta = -\ln \tan(\theta/2)$ , approaches  $\pm \infty$  along and 0 orthogonal to the beamline

489 distance  $\Delta R = \sqrt{\Delta\eta^2 + \Delta\phi^2}$

490 transverse energy  $E_T = \sqrt{p_T^2 + m^2}$

491 transverse momentum  $p_T$  component of momentum orthogonal to the beam axis  $p_T =$

492  $\sqrt{p_x^2 + p_y^2}$

### 493 3.2.1 Inner detector

494 • measures tracks of charged particles with high momentum resolution ( $\sigma_{p_T}/p_T =$   
495  $0.05\% \pm 1\%$ )

496 • covers particles with  $p_T > 0.5$  GeV,  $|\eta| < 2.5$

497 pixel detector -> semiconductor tracker -> transition radiation tracker, innermost to  
498 outermost

499 • pixel detector:

500 – innermost, 250  $\mu\text{m}$  silicon pixel layers

- 501           – detects charged particles from electron-hole pair production in silicon
- 502           – measures impact parameter resolution & vertex identification for reconstruction
- 503           of short-lived particles
- 504           – spatial resolution of 10  $\mu\text{m}$  in the  $R - \phi$  plane and 115  $\mu\text{m}$  in the z-direction
- 505           – 80.4m readout channels
- 506       • sct:
- 507           – surrounds pixel detector, silicon microstrip layers with 80  $\mu\text{m}$  strip pitch
- 508           – particle tracks cross 8 strip layers
- 509           – measures particle momentum, impact parameters, vertex position
- 510           – spatial resolution of 17  $\mu\text{m}$  in the  $R - \phi$  plane and 580  $\mu\text{m}$  in the z-direction
- 511           – 6.3m readout channels.
- 512       • trt:
- 513           – outermost, layers of 4 mm diameter gaseous straw tubes with transition radiation
- 514           material (70%  $Xe$  + 27%  $CO_2$  + 3%  $O_2$ ) & 30  $\mu\text{m}$  gold-plated wire in the center
- 515           – tubes 144 cm length in barrel region ( $|\eta| < 1$ ), 37 cm in the endcap region ( $1 <$
- 516            $|\eta| < 2$ ), arranged in wheels instead of parallel to beamline)
- 517           – gas mixture produces transition radiation when ionized for electron identification
- 518           – resolution/accuracy of 130  $\mu\text{m}$  for each straw tube in the  $R - \phi$  plane
- 519           – 351k readout channels

### 520 3.2.2 Calorimeter systems

521 surrounds the inner detector & solenoid magnet, covers  $|\eta| < 4.9$  and full  $\phi$  range. Alternates  
522 passive and active material layers. Incoming particles passing through calorimeter produce  
523 EM cascades or hadronic showers in passive layer. Energies deposited and convert to electric  
524 signals in active layers for readout.

525

526 EM calorimeter:

541

range for electrons/photons & precision

- 527 • innermost, lead-LAr detector (passive-  
542  
528 active)

physics, coarser elsewhere for jet recon-  
543 struction & MET measurements

- 529 • measures EM cascades (bremsstrahlung  
544  
530 & pair production) produced by elec-  
545 trons/photons

hadronic calorimeter:

- 531  
532 • divided into barrel region ( $|\eta| < 1.47$ )  
546  
533 & endcap regions ( $1.375 < |\eta| < 3.2$ )  
548  
534 with transition region ( $1.372 < |\eta| <$   
549  
535 1.52) containing extra cooling materi-  
550  
536 als for inner detector

• outermost  
546  
• measures hadronic showers from inelas-  
547  
tic QCD collisions

- 537 • end-cap divided into outer wheel  
552  
538 ( $1.372 < |\eta| < 2.5$ ) & inner wheel  
553  
539 ( $2.5 < |\eta| < 3.2$ )  
554  
• higher granularity in ID ( $|\eta| < 2.5$ )

• thick enough to prevent most particles  
548  
showers from reaching muon spectrom-  
549  
eter

• split into tile calorimeter in barrel re-  
551 gion ( $|\eta| < 1.0$ ) & extended barrel re-  
552 gion ( $0.8 < |\eta| < 1.7$ ), LAr hadronic  
553 end-cap calorimeter (HEC) in end-cap  
regions ( $1.5 < |\eta| < 3.2$ ) & LAr forward

556 calorimeters (FCal) in  $3.1 < |\eta| < 4.9$   
 557 range. 564

- LAr. overlap with other calorimeter systems to cover for gaps between subsystems
- fcal: 1 copper module & 2 tungsten modules-LAr. copper optimized for EM measurements, tungsten for hadronic.

### 570 3.2.3 Muon spectrometer

- ATLAS outermost layer. measures muon momenta & charge in range  $|\eta| < 2.7$
  - momentum measured by deflection in track from toroid magnets producing magnetic field orthogonal to muon trajectory
    - large barrel toroids in  $|\eta| < 1.4$ , strength 0.5 T
    - 2 smaller end-cap toroids in  $1.6 < |\eta| < 2.7$ , strength 1 T
    - transition region  $1.4 < |\eta| < 1.6$ , deflection provided by a combination of barrel and end-cap magnets
  - chambers installed in 3 cylindrical layers, around the beam axis in barrel region & in planes perpendicular to beam axis in the transition and end-cap regions
  - split into high-precision tracking chambers (monitored drift tubes & cathode strip chambers) & trigger chambers (resistive plate chambers & thin gap chambers)

- 582     • trigger chambers provide fast muon multiplicity & approximate energy range informa-  
 583        tion with L1 trigger logic

584     — mdt:  
 585        \* range  $|\eta| < 2.7$ , innermost layer<sup>606</sup>  
 586         $|\eta| < 2.0$ <sup>607</sup>  
 587        \* precision momentum measure-  
 588              ment  
 589        \* layers of 30 mm drift tubes filled  
 590              with 93% Ar & 7% CO<sub>2</sub>, with  
 591              a 50  $\mu\text{m}$  gold-plated tungsten-  
 592              rhenium wire at the center<sup>608</sup>  
 593        \* muons pass through tube, ion-  
 594              609  
 595              610  
 596              611  
 597              612  
 598              613  
 599              614  
 600              615  
 601     — CSC:  
 602        \* forward region  $2.0 < |\eta| < 2.7$   
 603              highest particle flux and density<sup>616</sup>  
 604              region  
 605        \* multiwire proportional chambers  
 606              with higher granularity, filled  
 607              with 80% Ar & 20% CO<sub>2</sub>  
 608              \* shorter drift time than MDT,  
 609              plus other features making CSC  
 610              suitable for high particle den-  
 611              sities and consequently able to  
 612              handle background conditions

617 — rpc:  
618      \* range  $|\eta| < 1.05$   
619      \* provide fast meas  
620 — tgc:  
621      \* range  $1.05 < |\eta| < 2.7$

### 622 3.2.4 Forward detectors

- 623 • LUCID (LUminosity measurement using Cherenkov Integrating Detector):  $\pm 17$  m from  
624 interaction point, measures luminosity using  $pp$  scattering in the forward region
- 625 • ALFA (Absolute Luminosity for ATLAS):  $\pm 240$  m, measures  $pp$  scattering at small  
626 angles
- 627 • ZDC (Zero-Degree Calorimeter):  $\pm 140$  m, measures centrality in heavy-ion collisions

### 628 3.2.5 Magnetic systems

- 629 superconducting solenoid & toroid magnets cooled to 4.5 K with liquid helium  
630 solenoid: 2.56 m diameter, 5.8 m length, 2 T strength axial magnetic field, encloses inner  
631 detector  
632 toroid = barrel + endcap toroid x2  
633 barrel toroid: 9.2/20.1 m inner/outer diameter, 25.3 m length, 0.5 T strength  
634 endcap toroid: 1.65/10.7 m inner/outer diameter, 5 m length, 1 T strength  
635 (show magnet system diagram)

### 636 3.2.6 Trigger & data acquisition

- 637 LHC produces large amount of data (40 MHz with 25 ns bunch crossing), necessitates a way  
638 to filter out trash from interesting events

639 handles online processing, selecting and recording interesting events for further offline pro-  
640 cessing and more in-depth analyses

641

- 642 • Level-1 (L1) trigger: online, fast hardware-based trigger, reduces to 100 kHz
- 643     – L1 calorimeter triggers (L1Calo): selects high energy objects & MET
- 644     – L1 muon triggers (L1Muon): selects using hit information from RPC & TGC
- 645     – L1 topological trigger (L1Topo): select based on topological selection synthesized
- 646         using information from L1Calo & L1Muon
- 647     – Central Trigger Processor (CTP): uses L1Calo/Muon/Topo for final L1 trigger
- 648         decision within  $2.5 \mu\text{s}$  latency. Also identify regions of interest in  $\eta$  and  $\phi$  to be
- 649         processed directly by HLT
- 650 • L1 trigger information read out by Front-End (FE) detector electronics then sent to
- 651         ReadOut Drivers (ROD) for preprocessing and subsequently to ReadOut System (ROS)
- 652         to buffer
- 653 • High-Level Trigger (HLT): offline, software-based trigger, using dedicated algorithms
- 654         and L1 output as input, reduces to 1 kHz
- 655 • Send to storage for analyses after HLT

656 overall trigger process reduces original collision data rate by a factor of about 10000 after  
657 HLT  
658 (show TDAQ diagram)

659 **Chapter 4. Data & Simulated Samples**

660 **4.1 Data samples**

661 LHC Run 2 data collected at  $\sqrt{s} = 13$  TeV between 2015-2018

662 luminosity  $140 \text{ fb}^{-1}$

663 (include uncertainty for Run 2 only)

Triggers used:

Table 4.1: Caption

Trigger	Data period			
	2015	2016	2017	2018
Single electron triggers				
HLT_e24_lhmedium_L1EM20VH	✓	-	-	-
HLT_e60_lhmedium	✓	-	-	-
HLT_e120_lhloose	✓	-	-	-
HLT_e26_lhtight_nod0_ivarloose	-	✓	✓	✓
HLT_e60_lhmedium_nod0	-	✓	✓	✓
HLT_e140_lhloose_nod0	-	✓	✓	✓
Di-electron triggers				
HLT_2e12_lhloose_L12EM10VH	✓	-	-	-
HLT_2e17_lhvloose_nod0	-	✓	-	-
HLT_2e24_lhvloose_nod0	-	-	✓	✓
HLT_2e17_lhvloose_nod0_L12EM15VHI	-	-	-	✓
Single muon trigger				
HLT_mu20_iloose_L1MU15	✓	-	-	-
HLT_mu40	✓	-	-	-
HLT_mu26_ivarmedium	-	✓	✓	✓
HLT_mu50	-	✓	✓	✓

664

665 **4.2 Monte Carlo samples**

666 Monte Carlo simulated samples are used to estimate signal acceptance before unblinding,  
667 profile the physics background for the analysis and to study object optimizations.  
668 Simulated samples for this analysis use are generated from ATLAS' generalized MC20a/d/e  
669 samples for Run 2, using full detector simulation (FS) based on Geant4.

670 **4.2.1  $t\bar{t}Z'$  signal samples**

671 Run 2  $t\bar{t}Z'$  sample  
672 samples: 6 samples for each mass point from [1, 1.25, 1.5, 2, 2.5, 3] TeV  
673 generator: MADGRAPH5\_AMC@NLO v.2.8.1p3.atlas9 at LO with NNPDF3.1LO pdf  
674 event: PYTHIA8 [v.244p3.rangefix] using A14 tune & NNPDF2.3LO pdf  
675 parameters:

- 676 • chirality  $\theta$ : does not affect the strong production mode for  $t\bar{t}Z'$ , therefore picking  
677 default value  $\pi/4$  to suppress loop-production of the  $Z'$  resonance
- 678 • top- $Z'$  coupling  $c_t = 1$

679 resonance width computed with MADGRAPH5\_AMC@NLO to be 4% of model configuration  
680 with these parameters

681 **4.2.2 Background samples**

682 Run 2 mc20 samples (2015-2018)  
683 (explain most important backgrounds:  $t\bar{t}t\bar{t}$  &  $t\bar{t}t$ ,  $t\bar{t}V$ ,

Table 4.2: Summary of all Monte-Carlo samples used in this analysis.

Process	ME Generator	ME Order	ME PDF	PS	Tune	Sim.
<b>Signals</b>						
$t\bar{Z}'/tjZ'/tWZ'$	MADGRAPH5_AMC@NLO LO		NNPDF3.1LO	PYTHIA8 A14		FS
<b><math>t\bar{t}t\bar{t}</math> and <math>t\bar{t}t</math></b>						
$t\bar{t}t\bar{t}$	MADGRAPH5_AMC@NLO NLO MADGRAPH5_AMC@NLO NLO	NLO	NNPDF3.0nlo MMHT2014LO	PYTHIA8 A14 HERWIG7 H7-UE-MMHT	AF3 AF3	
$t\bar{t}t$	SHERPA	NLO	NNPDF3.0 NNLO	HERWIG7 SHERPA	FS	
$t\bar{t}t$	MADGRAPH5_AMC@NLO LO		NNPDF2.3lo	PYTHIA8 A14	AF3	
<b><math>t\bar{t}V</math></b>						
$t\bar{t}H$	POWHEGBOX v2	NLO	NNPDF3.0nlo (mc20) PDF4LHC21 (mc23)	PYTHIA8 A14	FS AF3	
	POWHEGBOX v2	NLO	NNPDF3.0nlo	HERWIG7 H7.2-Default	FS	
$t\bar{t}Z$	MADGRAPH5_AMC@NLO NLO		NNPDF3.0 NNLO	PYTHIA8 A14	FS	
$t\bar{t}W$	SHERPA	NLO	NNPDF3.0 NNLO	SHERPA SHERPA	FS	
	SHERPA	LO	NNPDF3.0 NNLO	SHERPA SHERPA	FS	
<b><math>t\bar{t}</math> and Single-Top</b>						
$t\bar{t}$	POWHEGBOX v2	NLO	NNPDF3.0nlo	PYTHIA8 A14	FS	
$tW$	POWHEGBOX v2	NLO	NNPDF3.0nlo	PYTHIA8 A14	FS	
$t(q)b$	POWHEGBOX v2	NLO	NNPDF3.0nlo (s) NNPDF3.0nlo 4f (t)	PYTHIA8 A14	FS FS	
$tWZ$	MADGRAPH5_AMC@NLO NLO		NNPDF3.0nlo	PYTHIA8 A14	FS	
$tZ$	MADGRAPH5_AMC@NLO LO		NNPDF3.0nlo 4f	PYTHIA8 A14	FS	
<b><math>t\bar{t}VV</math></b>						
$t\bar{t}WW$	MADGRAPH5_AMC@NLO LO (mc20)		NNPDF3.0nlo	PYTHIA8 A14	FS	
	MADGRAPH (mc23)				FS	
$t\bar{t}WZ$	MADGRAPH	LO	NNPDF3.0nlo	PYTHIA8 A14	AF3	
$t\bar{t}HH$	MADGRAPH	LO	NNPDF3.0nlo	PYTHIA8 A14	AF3	
$t\bar{t}WH$	MADGRAPH	LO	NNPDF3.0nlo	PYTHIA8 A14	AF3	
$t\bar{t}ZZ$	MADGRAPH	LO	NNPDF3.0nlo	PYTHIA8 A14	AF3	
<b><math>V(VV)+jets</math> and <math>VH</math></b>						
$V+jets$	SHERPA	NLO	NNPDF3.0 NNLO	SHERPA SHERPA	FS	
$VV+jets$	SHERPA	NLO	NNPDF3.0 NNLO	SHERPA SHERPA	FS	
		LO ( $gg \rightarrow VV$ )			FS	
$VVV+jets$	SHERPA	NLO	NNPDF3.0 NNLO	SHERPA SHERPA	FS	
$VH$	POWHEGBOX v2	NLO	NNPDF3.0 AZNLO	PYTHIA8 A14	FS	

# 684 Chapter 5. Particle Reconstruction & Identifi- 685 fication

686 Reconstruction software reconstructs basic objects from signals collected from the event:  
687 interaction vertices, tracks, topological clusters of energy deposits  
688 These quantities then used to reconstruct physics objects i.e. particles (electron, muon),  
689 jets, MET

## 690 5.1 Primary reconstruction

### 691 5.1.1 Topological clusters

692 [19][20]

693 Topological cluster (topo-cluster): Clusters of topologically connected cell signals in the  
694 calorimeter at the EM scale. This scale does not consider loss of signal from hadrons. Sin-  
695 gular hits without hits from neighboring cells are considered noise.

696 Done in an effort to extract signal while minimizing electronic effects and physical fluctua-  
697 tions. Used to reconstruct hadronic objects and particles decaying hadronically i.e.  $\tau$  leptons

698 Signal hits with significance above a cell signal significance level  $\zeta_{\text{cell}}^{\text{EM}}$  are seeded in as part  
699 of a proto-cluster. Neighboring cells satisfying a cluster growth threshold are collected into  
700 the cluster.

701 Two clusters are merged if a cell is matched to both

702 If a cluster has two or more local signal maxima satisfying  $E_{\text{cell}}^{\text{EM}} > 500 \text{ MeV}$ , the cluster is  
703 split accordingly.

704 The process continues iteratively until all cells with significant signal efficiency have been  
705 matched to a cluster.

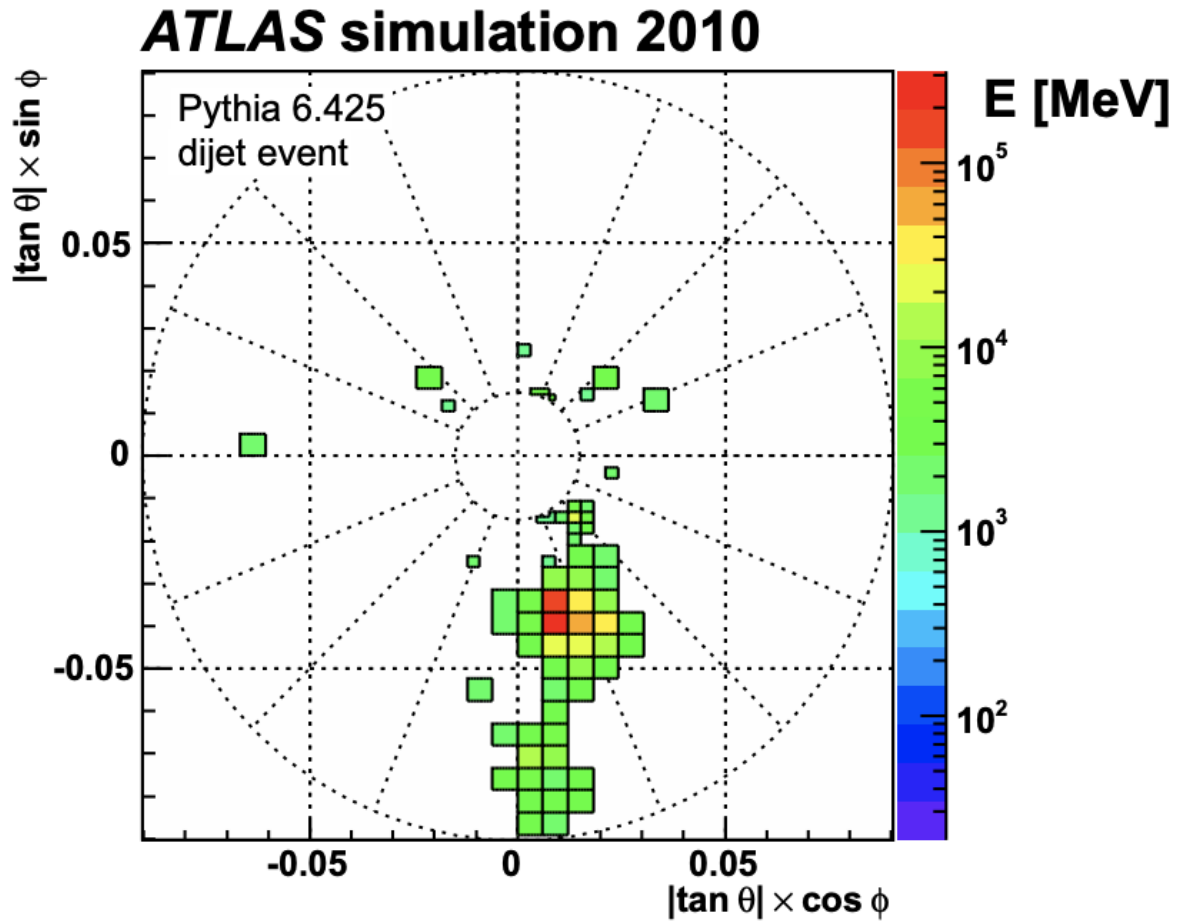


Figure 5.1

706

### 707 5.1.2 Tracks

708 [21]

709 Charged particles deposit energy in different layers of the inner detector and muon spec-  
710 trometer

711 ID reco software: inside-out and outside-in algorithms

712

- 713 • Inside-out: [22]

714 Starts with seeded hits in the silicon detector in pixel & SCT

715 Loosely matched to an EM cluster to form a track candidate

716 Hits are added to form a track candidate using a pattern recognition algorithm based  
717 on a Kalman filter formalism [23]

718 Track candidates are then fitted with a  $\chi^2$  filter [24] and loosely matched to a fixed-sized  
719 EM cluster. Successfully matched track candidates are re-fitted with a Gaussian-sum  
720 filter (GSF) [25]

721 This is followed by a track scoring strategy to resolve fake tracks & hit ambiguity  
722 between different tracks [26]

723 Extend to TRT to form final tracks, filtered by threshold  $p_T > 400$  MeV.

724

- 725 • Outside-in: [27]

726 Reverse, starts with segments in TRT extending inward to silicon hits in pixel & SCT

727 Targeting secondary tracks (decays/interactions of primary particles) or long-lived par-  
728 ticles

### 729 5.1.3 Vertices

730 Vertices: interaction or decay point

731 Primary vertex: pp interaction point

732 Important for reconstruction of the hard scattering pp interaction, resulting trajectories and

<sup>733</sup> kinematic information of the event

<sup>734</sup>

<sup>735</sup> • Vertex finding:

<sup>736</sup> Uses the z-position of a track as input

<sup>737</sup> Vertices require to have at least 2 tracks

<sup>738</sup> Iterative  $\chi^2$  algorithm evaluate track-vertex compatibility, using the track as new seed  
<sup>739</sup> for another vertex if large discrepancy

<sup>740</sup> • Vertex fitting:

<sup>741</sup> Adaptive multi-vertex fitter (AVF) algorithm assigns weights that depend on the track-  
<sup>742</sup> vertex compatibility to each track to measure the probability of the track being an  
<sup>743</sup> outlier vs inlier.

<sup>744</sup> Vertex is then estimated by iteratively minimizing an objective function of these  
<sup>745</sup> weights

## <sup>746</sup> 5.2 Jets

<sup>747</sup> - Quarks, gluons & other non-color-neutral hadrons cannot be observed individually due to

<sup>748</sup> QCD color confinement

<sup>749</sup> - A non-color-neutral hadron will almost immediately undergo hadronization producing a  
<sup>750</sup> cone of color-neutral hadrons also known as a jet

<sup>751</sup> - Jet signals can be used to reconstruct and consequently indirectly observe the original  
<sup>752</sup> quarks/gluons the jets originated from

<sup>753</sup> - Jet reconstruction:

- 754     • PFlow: energy deposited in the calorimeter systems by charged particles is removed  
 755       and replaced by particle objects created with the remaining energy in the calorimeter  
 756       and tracks matched to the topo-clusters. (include PFlow graphics)
- 757     • anti- $k_t$  algorithms: sequential recombination jet algorithms
- 758     • pile-up jets: multiple interactions associated with one bunch crossing in addition to the  
 759       hard scattering of interest and reconstructed as jets in the final states. Reconstructed  
 760       pile-up jets can result from Pile-up jets are usually from soft interactions and can be  
 761       distinguished with JVT algorithm using tracking information from the ID.
- 762     • JES/JER calibration: Jet reconstruction at EM scale does not accurately account  
 763       for energy from QCD interactions and needs to be calibrated to jets reconstructed at  
 764       particle level. This is done via a MC-based JES calibration sequence and additional  
 765       JER calibration to match jet resolution in simulation to data using dijet events.  
 766       For this analysis, jets are reconstructed using PFlow method with anti- $k_t$  algorithm,  
 767       using radius parameter  $\Delta R = 0.4$ .  
 768       JVT applied to reconstructed jets with  $p_T < 60$  GeV and  $|\eta| < 2.4$ .

### 769 5.2.1 Flavor tagging

- 770 - Classification of hadronic jets is an important task for many LHC analyses especially ones  
 771       studying final states (Higgs decay/4top)
- 772 - Flavor tagging is namely interested in identifying jets containing  $b$ -hadrons,  $c$ -hadrons,  
 773        $uds$ -hadrons (light-jets), and hadronic decays from  $\tau$ .
- 774 - Of these, identifying  $b$ -jets is of particular interest due to their characteristically long

<sup>775</sup> lifetime ( $\approx 1.5$  ps) from decay suppression by CKM factor, with a displaced secondary decay  
<sup>776</sup> vertex and usually a tertiary vertex from  $c$ -hadron decays.

## <sup>777</sup> Efficiency calibration

<sup>778</sup> - [28]

<sup>779</sup> - Performance of  $b$ -taggers are studied on MC simulated samples. However, the  $b$ -tagging  
<sup>780</sup> efficiency predicted by simulation  $\varepsilon_b^{\text{sim}}$  is usually not the same as the efficiency measured in  
<sup>781</sup> data  $\varepsilon_b^{\text{data}}$ .

<sup>782</sup> - The correction for the rate of events after applying a  $b$ -tagging requirement is calibrated  
<sup>783</sup> and applied jet by jet in the form of data-to-simulation scale factors  $\text{SF} = \varepsilon_b^{\text{data}} / \varepsilon_b^{\text{sim}}$ .

<sup>784</sup> - Usage of  $b$ -tagger in this analysis is done via five operating points (OPs), corresponding  
<sup>785</sup> to 60%, 70%, 77%, 85% and 90%  $b$ -jet tagging efficiency  $\varepsilon_b$  in simulated  $t\bar{t}$  events in order  
<sup>786</sup> from loosest to tightest discriminant cut points. - OPs are defined by selection on the tagger  
<sup>787</sup> output to provide a pre-defined level of  $\varepsilon_b$ , and act as a variable trade-off between  $b$ -tagging  
<sup>788</sup> efficiency and  $c$ -/light-jet rejection i.e.  $b$ -jet purity

<sup>789</sup> - A jet is considered  $b$ -tagged if it passes the efficiency criteria for a given OP. A pseudo-  
<sup>790</sup> continuous  $b$ -tagging (PCBT) score is defined to summarize the OP criteria a jet passes into  
<sup>791</sup> a variable. The PCBT score can take integer values between 1 and 6, where a score of 6  
<sup>792</sup> means a jet passes all four OP thresholds (passing 65% OP), a score of 2 for jets that pass  
<sup>793</sup> only the 90% OP, and a score of 1 for jets that don't pass any OP. Additionally, PCBT  
<sup>794</sup> defines a value of -1 for any jet that does not satisfy  $b$ -tagging criteria.

<sup>795</sup>

<sup>796</sup> - For this analysis,jets containing  $b$ -hadrons are identified and tagged with the GN2v01  
<sup>797</sup> algorithm, described in subsection 5.2.1. A jet is considered  $b$ -tagged if it passes the 85%

798 WP; this gives the best sensitivity to the signal out of all five possible  $b$ -tagging WPs. The  
799  $b$ -tagged jet is then assigned a PCBT score accordingly.

800 **btag optimization table?**

## 801 **GN2 $b$ -tagging algorithm**

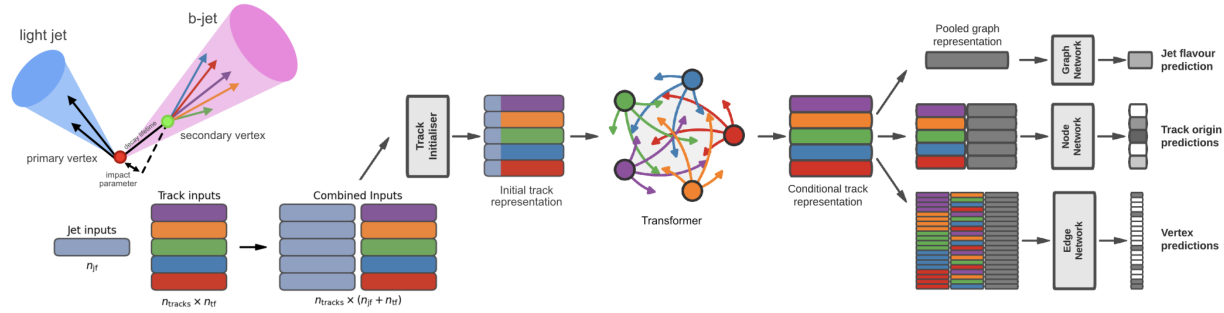


Figure 5.2: Caption [29–31]

802 - GN2 transformer-based  $b$ -tagging algorithm, utilized for analysis of Run 2 and Run 3

803 data

804 - GN2 gives a factor of 1.5-4 improvement in experimental applications compared to the  
805 previous convolutional neural network-based standard  $b$ -tagging algorithm, DL1d, without  
806 dependence on the choice of MC event generator.

807 - Attention-based architecture, modified to incorporate domain knowledge and additional  
808 auxiliary physics objectives: grouping tracks originating from common vertices and predic-  
809 tion of the underlying process for each track

810 - MC simulated SM  $t\bar{t}$  and BSM  $Z'$  events from  $pp$  collisions were used as training and  
811 evaluation samples. In order to minimize bias, both  $b$ - and light-jet samples are re-sampled  
812 to match  $c$ -jet distributions.

813 - GN2 concatenates 2 jet and 19 track reconstruction variables of up to 40 tracks to form

814 the input feature vector, normalized to zero mean and unit variance.  
815 - The output consists of a jet classification layer of size 4 consisting of  $p_b$ ,  $p_c$ ,  $p_u$  and  $p_\tau$  for  
816 the probability of each jet being a  $b$ -,  $c$ -, light- or  $\tau$ -jet respectively; a track-pairing output  
817 layer of size 2, and a track origin classification layer of 7 output categories.

## 818 5.3 Leptons

819 - Lepton reconstruction is concerned mainly with electron and muon construction, since tau  
820 decays quickly and can either be reconstructed using jets or light leptons. From here on out  
821 lepton will be used mostly to refer to electrons and muons  
822 - Leptons can be classified into two categories: prompt leptons resulting from heavy particle  
823 decays, or non-prompt leptons resulting from detector or reconstruction effects, or from  $b$ -  
824 or  $c$ - hadron decays  
825 - Reconstruction of leptons is therefore important to study the underlying physics and sup-  
826 pressing background

### 827 5.3.1 Electrons

828 - [32][33]  
829 - Electrons lose energy interacting with the detector materials via bremsstrahlung. The  
830 bremsstrahlung photon can then produce an electron-positron pair which can itself leaves  
831 signals in the detector, creating a collimated object that can leave multiple tracks in the ID  
832 or EM showers in the calorimeter, all considered part of the same EM topo-cluster.  
833 - Electron signal signature has three characteristic components: localized energy deposits in  
834 the calorimeter, multiple tracks in the ID and compatibility between the above tracks and

835 energy clusters in the  $\eta \times \phi$  plane. Electron reconstruction in ATLAS follows these steps ac-  
cordingly - Seed-cluster reconstruction and track reconstruction are performed sequentially

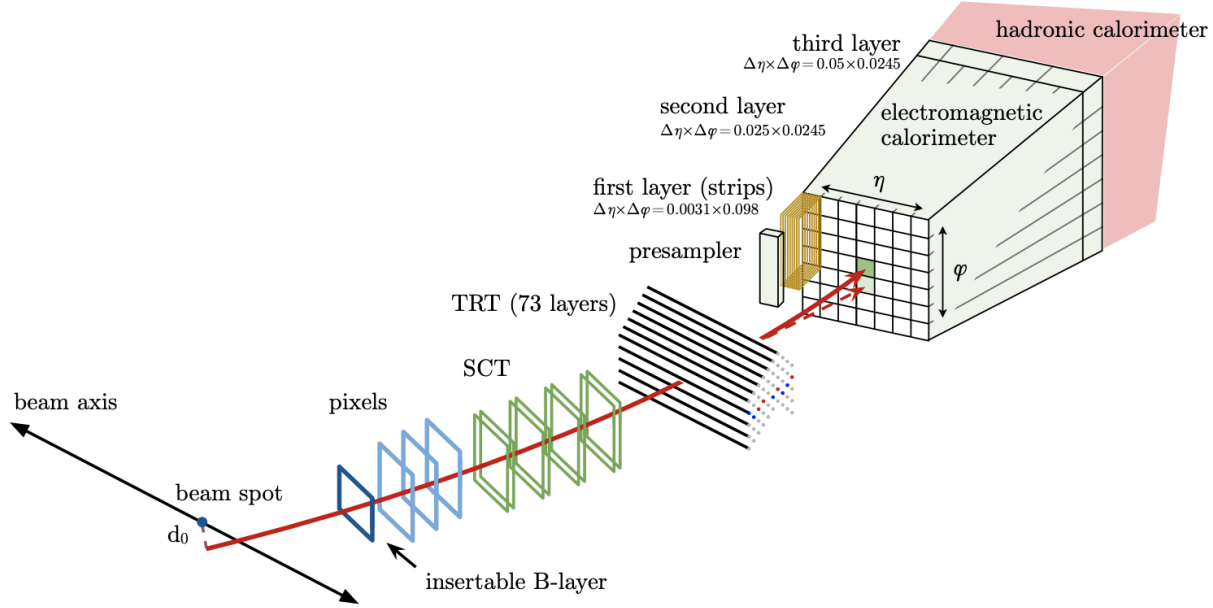


Figure 5.3: Caption [32]

836

837 in accordance with the iterative clustering algorithm and track reconstruction method re-

838 spectively, described in section 5.1

839 - The seed-cluster and track candidate associated with a conversion vertex are then matched

840 to form an electron candidate.

841 - A reconstructed cluster is expanded from the seed-cluster in either  $\phi$  or  $\eta$  in the barrel or

842 endcap region respectively

843 - The cluster energy is then calibrated to compute the original electron energy.

#### 844 Electron identification

845 - Additional likelihood-based identification selections using ID and EM calorimeter infor-

846 mation are implemented to further improve the purity of the reconstructed electrons and

847 photons. These selections also help suppress background from hadronic jet deposits, photon  
848 conversions or electrons from heavy-flavor decays.

849 - Three operating points are defined for physics analyses: Loose, Medium and Tight, op-  
850 timized for 9 bins in  $|\eta|$  and 12 bins in  $E_T$  with each corresponding to a fixed efficiency  
851 requirement for each bin. The target efficiencies for Loose, Medium and Tight start at 93%,  
852 88% and 80% respectively for typical EW processes and increases with  $E_T$   
853 Similar to  $b$ -tagging OPs, the electron OPs represent a trade-off in signal efficiency and back-  
854 ground rejection. The electron efficiency are estimated using tag-and-probe method [32] on  
855 samples of  $J/\Psi \rightarrow ee$  and  $Z \rightarrow ee$ [33].

856 **Electron isolation**

- A characteristic distinction between prompt electrons and electrons from background pro-  
cesses is the relative lack of activity in both the ID and calorimeter within an area of  $\Delta\eta \times \Delta\phi$   
surrounding the reconstruction candidate

- Electron isolation variables are needed to quantify the amount of activity around the elec-  
tron candidate.

- Calorimeter-based isolation variables  $E_T^{\text{cone}XX}$  is calculated by first summing the energy of  
topological clusters with barycenters falling within a cone of radius  $\Delta R = \sqrt{(\Delta\eta)^2 + (\Delta\phi)^2} =$   
 $XX/100$  around the direction of the electron candidate.

- The final isolation variable is then obtained by subtracting energy at the core of the cone  
belonging to the candidate electron from the sum, then applying corrections for energy leak-  
age outside of the core and pile-up effects.

- Similar to calorimeter-based variables, track-based isolation variables  $p_T^{\text{varcone}XX}$  are cal-  
culated by summing all track  $p_T$  within a cone of variable radius  $\Delta R$  around the electron

candidate, minus the candidate's contribution. The cone radius is variable as a function of

$p_T$

$$\Delta R = \min \left( \frac{10}{p_T[\text{GeV}]}, \Delta R_{\max} \right)$$

with  $\Delta R_{\max}$  being the maximum cone size, to account for the closer proximity of decay products to the electron in high-momentum heavy particle decays.

- Four isolation operating points are implemented to satisfy specific needs by physics analyses:  
Loose, Tight, HighPtCaloOnly and Gradient. The first three OPs are fixed in isolation variables, while the Gradient OP fixes the isolation efficiency to a  $p_T$  dependent function defined as  $\varepsilon = 0.1143 \times p_T + 92.14\%$  with  $p_T$  in GeV, using  $\Delta R = 0.2$  for calorimeter isolation and  $\Delta R_{\max} = 0.2$  for track isolation[33].

## Electron charge misidentification

[32][34]

Electron charge is determined by the curvature of the associated track. Misidentification of charge can then occur via either an incorrect curvature measurement, or an incorrectly matched track.

The former is more likely for electrons with high  $p_T$  due to the small curvature in track trajectories at such scale, while the latter usually results from bremsstrahlung pair-production, creating additional secondary tracks in the vicinity.

Charge misidentification is a crucial irreducible background for analyses with charge selection criteria, and suppression of this background is assisted via a boosted decision tree discriminant known as the Electron Charge ID Selector (ECIDS) [32]. The addition of ECIDS removed 90% of electrons with incorrect charge while selecting 98% of electrons with correct

charge from electrons in  $Z \rightarrow ee$  events satisfying Medium/Tight identification and Tight isolation criteria.

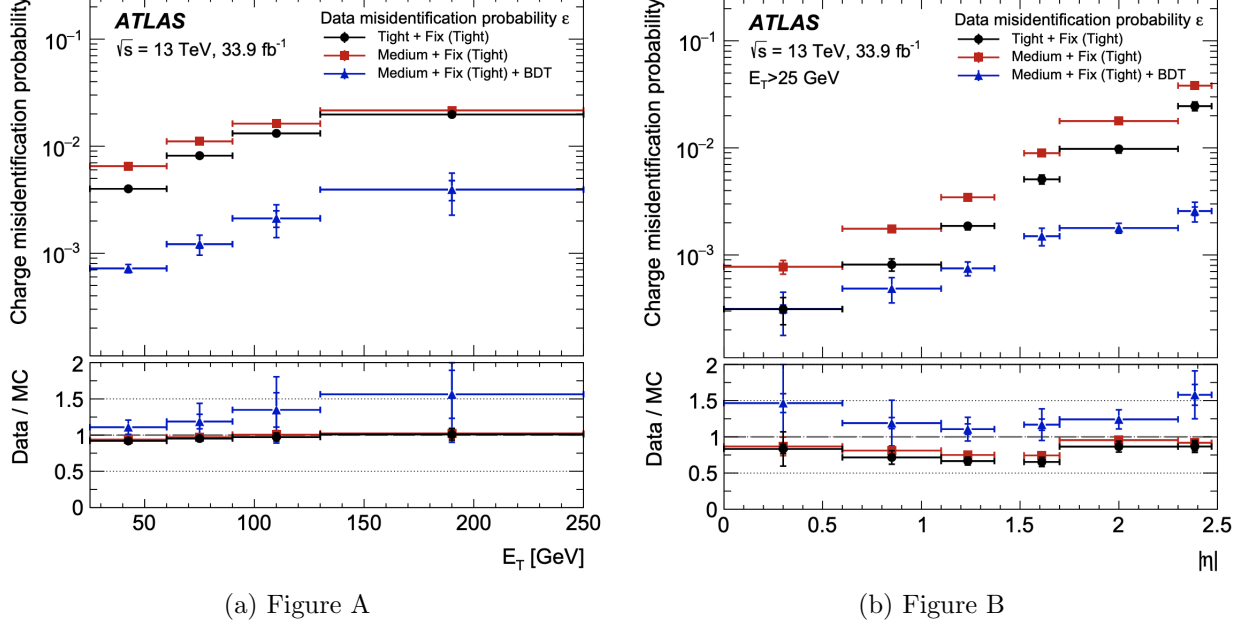


Figure 5.4: Caption [33]

877

### 878 5.3.2 Muons

879 Signature: minimum-ionizing particle leaves tracks in the MS or characteristics energy de-  
880 posits in the calorimeter

881 Muons can be reconstructed globally using information from the ID, MS and calorimeters.

882 Five reconstruction strategies, each corresponding to a muon type:

- 883 • Combined (CB): primary ATLAS muon reconstruction method. Muons first recon-  
884 structed using MS tracks then extrapolated to include ID tracks (outside-in strategy).

885 A global combined fit is then performed on both MS and ID tracks

- 886 • Inside-out combined (IO): Complementary to CB algorithm. Muon tracks are extrap-

887       olated from ID to MS, then fitted together with a combined track fit. Useful for muons  
888       without good MS information.

- 889     • MS extrapolated (ME): ME muons are defined as muons with a MS track that cannot  
890       be matched to an ID track using CB method. ME muons allow extension of muon  
891       reconstruction acceptance to regions not covered by the ID ( $2.5 < |\eta| < 2.7$ )
- 892     • Segment-tagged (ST): ST muons are ID tracks satisfying tight angular matching cri-  
893       teria to at least one reconstructed local segment in the MDT or CSC chambers when  
894       extrapolated to the MS. Used primarily when muons only crossed one layer of MS  
895       chambers.
- 896     • Calorimeter-tagged (CT): CT muons are ID tracks that when extrapolated through the  
897       calorimeter, can be matched to energy deposits consistent with those of a minimum-  
898       ionizing particle. Extends acceptance range to regions in the MS with sparse instrumen-  
899       tation ( $|\eta| < 0.1$ ), with a higher  $p_T$  threshold of 5 GeV compared to 2 GeV threshold  
900       used by other muon reconstruction algorithms due to large background contamination  
901       at the low  $p_T$  range of  $15 < p_T < 100$  GeV

902     **Muon identification**

903     [35][36]

904     Reconstructed muons are further filtered by identification criteria to select for high-quality  
905       prompt muons for physics analyses. Requirements include number of hits in the MS/ID,  
906       track fit properties and compatibility between measurements of the two systems.  
907     Three standard WPs (Loose, Medium, Tight) are defined to better match the needs of differ-  
908       ent physics analyses concerning prompt muon ID efficiency,  $p_T$  resolution and non-prompt

909 muon rejection. Of the three, Medium WP is the default ID WP for ATLAS, by virtue  
910 of being optimized in efficiency and purity for a wide range of analyses while minimizing  
911 non-prompt rejection and systematic uncertainties[[35](#)].

912

### 913 Muon isolation

914 Muons from heavy particle decays are often produced in an isolated manner compared to  
915 muons from semileptonic decays. Muon isolation is therefore an important tool for back-  
916 ground rejection in physics analyses

917 Muon isolation strategies are similar to that of electron in Figure 5.3.1, with track-based  
918 and calorimeter-based isolation variables.

919 Seven isolation WPs are defined to satisfy analyses' needs.

## 920 5.4 Missing transverse momentum

921 [[37](#)]

922 Collisions at the LHC happen along the z-axis of the ATLAS coordination system between  
923 two particle beam of equal center-of-mass energy. By conservation of momentum, the sum  
924 of transverse momenta of outgoing particles should be zero. A discrepancy between mea-  
925 sured momentum and zero would then suggest the presence of undetectable particles, which  
926 would consist of either SM neutrinos or some unknown BSM particles. This makes missing  
927 transverse momentum ( $E_T^{\text{miss}}$ ) an important observable to reconstruct.

928 Reconstructing  $E_T^{\text{miss}}$  utilizes information from fully reconstructed leptons, photons, jets  
929 and other matched track-vertex objects not associated with a prompt object (soft signals),

930 defined with respect to the  $x(y)$ -axis as

$$E_{x(y)}^{\text{miss}} = - \sum_{i \in \{\text{hard objects}\}} p_{x(y),i} - \sum_{j \in \{\text{soft signals}\}} p_{x(y),j}, \quad (5.1)$$

where  $p_{x(y)}$  is the  $x(y)$ -component of  $p_T$  for each particle. The following observables can then be defined:

$$\mathbf{E}_T^{\text{miss}} = (E_x^{\text{miss}}, E_y^{\text{miss}}), \quad (5.2)$$

$$E_T^{\text{miss}} = |\mathbf{E}_T^{\text{miss}}| = \sqrt{(E_x^{\text{miss}})^2 + (E_y^{\text{miss}})^2}, \quad (5.3)$$

$$\phi^{\text{miss}} = \tan^{-1}(E_y^{\text{miss}}/E_x^{\text{miss}}), \quad (5.4)$$

931 where  $E_T^{\text{miss}}$  represents the magnitude of the missing transverse energy vector  $\mathbf{E}_T^{\text{miss}}$ , and

932  $\phi^{\text{miss}}$  its direction in the transverse plane. Since physics analyses have differing requirements

933 for object selection, the vectorial sum  $\mathbf{E}_T^{\text{miss}}$  can be broken down into

$$\mathbf{E}_T^{\text{miss}} = - \underbrace{\sum_{\substack{\text{selected} \\ \text{electrons}}} \mathbf{p}_T^e - \sum_{\substack{\text{selected} \\ \text{muons}}} \mathbf{p}_T^\mu - \sum_{\substack{\text{accepted} \\ \text{photons}}} \mathbf{p}_T^\gamma - \sum_{\substack{\text{accepted} \\ \tau\text{-leptons}}} \mathbf{p}_T^\tau}_{\text{hard term}} - \underbrace{\sum_{\substack{\text{accepted} \\ \text{jets}}} \mathbf{p}_T^{\text{jet}} - \sum_{\substack{\text{unused} \\ \text{tracks}}} \mathbf{p}_T^{\text{track}}}_{\text{soft term}}. \quad (5.5)$$

934 Two WPs are defined for  $E_T^{\text{miss}}$ , Loose and Tight [38], with selections on jet  $p_T$  and JVT

935 criteria. The Tight WP is used in this analysis, and reduces pileup dependence of  $E_T^{\text{miss}}$  by

936 removing the phase space region with more pileup jets than hard-scatter jets, at the expense

937 of resolution at low pileup and scale of the reconstructed  $E_T^{\text{miss}}$ .

<sub>938</sub> **5.5 Overlap removal**

<sub>939</sub> Since the reconstruction processes for different objects are performed independently, it is  
<sub>940</sub> possible for the same detector signals to be used to reconstruct multiple objects. An overlap  
<sub>941</sub> removal strategy to resolve ambiguities; the overlap removal process for this analysis applies  
<sub>942</sub> selections listed in Table 5.1 sequentially, from top to bottom.

Table 5.1: Caption [39]

Remove	Keep	Matching criteria
Electron	Electron	Shared ID track, $p_{\text{T},1}^e < p_{\text{T},2}^e$
Muon	Electron	Shared ID track, CT muon
Electron	Muon	Shared ID track
Jet	Electron	$\Delta R < 0.2$
Electron	Jet	$\Delta R < 0.4$
Jet	Muon	( $\Delta R < 0.2$ or ghost-associated) & $N_{\text{track}} < 3$
Muon	Jet	$\Delta R < \min(0.4, 0.04 + 10\text{GeV}/p_{\text{T}}^{\mu})$

<sub>943</sub> **5.6 Object definition**

<sub>944</sub> Table 5.2 shows the selections used in this analysis. Each selection comes with associated  
<sub>945</sub> calibration scale factors to account for discrepancies between data and MC simulation, and  
<sub>946</sub> are applied multiplicatively to the MC event weights.

Table 5.2: Caption

Selection	Electrons	Muons	Jets
$p_T$ [GeV]	$> 15$ $p_T(l_0) > 28$	$> 15$	$> 20$
$ \eta $	$1.52 \leq  \eta  < 2.47$ $< 1.37$	$< 2.5$	$< 2.5$
Identification	TightLH pass ECIDS ( $ee/e\mu$ )	Medium	NNJvt FixedEffPt ( $p_T < 60$ , $ \eta  < 2.4$ )
Isolation	Tight_VarRad	PflowTight_VarRad	
Track-vertex assoc.			
$ d_0^{\text{BL}}(\sigma) $	$< 5$	$< 3$	
$ \Delta z_0^{\text{BL}} \sin \theta $ [mm]	$< 0.5$	$< 0.5$	

947 **Chapter 6. Analysis Strategy**

948 **6.1 Event selection**

949 Events for the analysis first are preselected following a list of criteria to optimize for event  
950 quality and background rejection.

951 The criteria are applied sequentially, from top to bottom

952 1. **Good Run List (GRL)**: data events must be part of a predefined list of suitable  
953 runs and luminosity blocks.

954 2. **Calorimeter cleaning**: events containing signal hits indicating an error in the calorime-  
955 ter are removed.

956 3. **Primary vertex**: events must have at least one reconstructed vertex matched to 2 or  
957 more associated tracks with  $p_T > 500$  MeV.

958 4. **Trigger**: events must be selected by at least one trigger documented in ??.

959 5. **Jet cleaning**: events must pass the LooseBad WP for jet cleaning using jets passing  
960 preselection criteria in section 5.6. This is done to remove events with significant  
961 number of calorimeter hits from non-prompt sources (e.g. instrumental effects, cosmic  
962 ray background, non-collision particles)

963 6. **Bad muon veto**: events are removed if they contain at least one muon before overlap  
964 removal with insufficient  $p_T$  resolution.

965 7. **Kinematic selection**: events must have exactly two Tight leptons with the same  
966 electric charge, or at lease three Tight leptons of any charge. The leading lepton must

967 have  $p_T > 28$  GeV, and all leptons must satisfy  $p_T > 15$  GeV.

968 Events are separated into two channels based on the number of leptons: same-sign di-lepton  
969 (SS2L) for events with exactly two leptons of the same charge, or multilepton (ML) for  
970 events with three or more leptons. The channels are further separated into regions defined  
971 in section 6.2 to prepare for analysis.

972 Further selections are applied based on the lepton flavors present. In the SS2L channel, if  
973 both leptons are electrons, the invariant mass  $m_{ll}$  must satisfy  $m_{ll} < 81$  GeV and  $m_{ll} > 101$   
974 GeV to suppress background involving  $Z$ -bosons. In the ML channel, the same criteria must  
975 be satisfied for every opposite-sign same-flavor pair of leptons in an event.

## 976 Event categorization

977 Simulated events are categorized using truth information of leptons ( $e/\mu$ ) and their origi-  
978 nating MC particle (mother-particle).

979 Each lepton can be classified as either prompt or non-prompt, with non-prompt leptons fur-  
980 ther categorized for background estimation purposes.

981 If an event contains only prompt leptons, the event is classified as its corresponding process.  
982 If the event contains one non-prompt lepton, the event is classified as the corresponding type  
983 of the non-prompt lepton. If the event contains more than one non-prompt lepton, the event  
984 is classified as other.

985 • **Prompt:** if the lepton originates from  $W/Z/H$  boson decays, or from a mother-  
986 particle created by a final state photon.

987 • **Non-prompt:**

- **Charge-flip ( $e$  only)**: if the reconstructed charge of the lepton differs from that of the first mother-particle.
- **Material conversion ( $e$  only)**: if the lepton originated from a photon conversion and the mother-particle is an isolated prompt photon, non-isolated final state photon, or heavy boson.
- **$\gamma$ -conversion ( $e$  only)**: if the lepton originated from a photon conversion and the mother-particle is a background electron.
- **Heavy flavor decay**: if the lepton originated from a  $b$ - or  $c$ -hadron.
- **Fake**: if the lepton originated from a light- or  $s$ -hadron, or if the truth type of the lepton is hadron.
- **Other**: any lepton that does not belong to one of the above categories.

## 6.2 Analysis regions

Events are selected and categorized into analysis regions belonging to one of two types: control regions (CRs) enriched in background events, and signal regions (SRs) enriched in signal events. This allows for the examination and control of backgrounds and systematic uncertainties, as well as study of signal sensitivities.

The signal is then extracted from the SRs with a profile LH fit using all regions. The full selection criteria for each region are summarized in Table 6.3

<sub>1006</sub> **6.2.1 Signal regions**

<sub>1007</sub> [include blinding strategy]

<sub>1008</sub> - All events selected for SS2L and 3L signal regions must satisfy the following criteria:

<sub>1009</sub>     • Contains 6 or more jets, with at least 2 jets  $b$ -tagged at the 85% WP

<sub>1010</sub>     • Scalar sum of the transverse momenta of all leptons and jets  $H_T > 500$  GeV

<sub>1011</sub>     • Dilepton invariant mass  $m_{\ell\ell}$  does not coincide with the  $Z$ -boson mass range of 81 – 101

<sub>1012</sub>           GeV

<sub>1013</sub> - The SR is further granularized by the number of  $b$ -jets and leptons to further study and

<sub>1014</sub> improve signal sensitivity

<sub>1015</sub>

Table 6.1: Caption

SR	Selection criteria	
	$b$ -jets	leptons
2b2l	$N_b = 2$	$N_l = 2$
2b3l4l	$N_b = 2$	$N_l \geq 3$
3b2l	$N_b = 3$	$N_l = 2$
3b3l4l	$N_b = 3$	$N_l \geq 3$
4b	$N_b = 4$	

<sub>1016</sub> **6.2.2 Control regions**

<sub>1017</sub> Control regions are defined for each background to be enriched in the targeted background

<sub>1018</sub> events, in order to maximize the targeted background's purity and minimize contamination

<sub>1019</sub> from other sources within the region.

1020 This helps to constrain and reduce correlation between background normalization factors.  
1021 Fit variables and selection criteria are determined via optimization studies on CRs to achieve  
1022 the largest discriminating power possible between the target background and other event  
1023 types.

1024  **$t\bar{t}W$  background CRs**

1025 Two types of CRs are defined to estimate the flavor composition and normalization of  $t\bar{t}W$   
1026 +jets background: CR  $t\bar{t}W^\pm$ +jets to constrain flavor composition, and CR 1b( $\pm$ ) to con-  
1027 strain jet multiplicity spectrum.  
1028 These are further split into CR  $t\bar{t}W^\pm$  and CR 1b( $\pm$ ) due to the pronounced asymmetry in  
1029  $t\bar{t}W$  production from  $pp$  collisions, with  $t\bar{t}W^+$  being produced at approximately twice the  
1030 rate of  $t\bar{t}W^-$ . Selections on  $H_T$  and  $N_{\text{jets}}$  to ensure orthogonality to SR  
1031 Selections on total charge for each charged  $W^\pm$  boson

1032

1033 **Fake/non-prompt background CRs**

1034 Selection for fake/non-prompt CRs are determined using the DFCommonAddAmbiguity (DF-  
1035 CAA) variable for reconstructed leptons.

Table 6.2: Caption

DFCAA	Description
-1	No 2nd track found
0	2nd track found, no conversion found
1	Virtual photon conversion candidate
2	Material conversion candidate

1036 Four CRs for three main types of fake/non-prompt backgrounds: virtual photon ( $\gamma^*$ )

<sub>1037</sub> conversion, photon conversion in detector material (Mat. Conv.) and heavy flavor decays  
<sub>1038</sub> (HF).

<sub>1039</sub>

- <sub>1040</sub> • Low  $m_{\gamma}^*$ : events with an  $e^+e^-$  pair produced from a virtual photon  
<sub>1041</sub> Selects two same-sign leptons with at least one electron reconstructed as an internal  
<sub>1042</sub> conversion candidate and neither as with a material conversion candidate ( $\text{DFCAA}_{\ell_1(\ell_2)} =$   
<sub>1043</sub> 1 and  $\neq 2$ )  
<sub>1044</sub> NF constrained using yield count only.
- <sub>1045</sub> • Mat. Conv.: events with an electron originating from photon conversion within the  
<sub>1046</sub> detector material.  
<sub>1047</sub> Selects two same-sign leptons with at least one electron reconstructed as a material  
<sub>1048</sub> conversion candidate ( $\text{DFCAA}_{\ell_1(\ell_2)} = 2$ ).  
<sub>1049</sub> NF constrained using yield count only.
- <sub>1050</sub> • HF  $e/\mu$ : events with a reconstructed non-prompt lepton from semi-leptonic decays of  
<sub>1051</sub>  $b$ - and  $c$ -hadrons (heavy flavor decays)  
<sub>1052</sub> Selects three leptons with at least two electrons/muons, with no lepton reconstructed  
<sub>1053</sub> as a conversion candidate ( $\text{DFCAA} < 0$ ).  
<sub>1054</sub> NFs constrained by fitting with  $p_T$  of the third leading lepton  $\ell_3$ .

### <sub>1055</sub> 6.2.3 Validation regions

<sub>1056</sub> In addition, validation regions are also defined to validate the normalization and modeling  
<sub>1057</sub> of  $t\bar{t}Z$  and  $t\bar{t}W$  background without being used in the fit.

- $t\bar{t}Z$ : Selects events with at least two  $b$ -tagged jets, at least four total jets and three leptons with at least one same-flavor opposite-sign lepton pair possessing invariant mass  $m_{\ell\ell}$  within the  $Z$ -boson mass window of  $81 - 101$  GeV
  - $t\bar{t}W$ : Main charge asymmetric background leaning  $t\bar{t}W^+$ , validated using the difference in number of positively and negatively charged events  $N_+ - N_-$  instead of total number of events.
- Selects using CR  $t\bar{t}W$  and CR 1b criteria, with one VR not orthogonal to SR and one orthogonal VR with more limited statistics.

## 6.3 Background estimation

- Background events in this analysis consist of SM processes that can result in a  $t\bar{t}t\bar{t}$  SSML final state.
- Can be divided into two types: reducible and irreducible.
- Reducible background consists of processes that do not result in SSML final state physically, but are reconstructed as such due to erroneous detector and reconstruction effects.
- Three main types: charge misidentification (QmisID), fake leptons and non-prompt leptons.
- Estimated using template fitting method to adjust MC predictions via floating normalization factors constrained in the CRs.
- Irreducible background consists of SM processes that result in SSML final states physically, with all leptons being prompt.
- Main irreducible background considered in this analysis:  $t\bar{t}t\bar{t}$ ,  $t\bar{t}W$ ,  $t\bar{t}Z$ , and  $t\bar{t}H$  with smaller contributions from  $VV$ ,  $VVV$ ,  $VH$  and rarer processes like  $t\bar{t}VV$ ,  $tWZ$ ,  $tZq$  and  $t\bar{t}H$ .

Table 6.3: Caption

Region	Channel	$N_{\text{jets}}$	$N_b$	Other selections	Fitted variable
CR Low $m_{\gamma^*}$	SS $e\ell$	[4, 6)	$\geq 1$	$\ell_1/\ell_2$ is from virtual photon decay $\ell_1 + \ell_2$ not from material conversion	event yield
CR Mat. Conv.	SS $e\ell$	[4, 6)	$\geq 1$	$\ell_1/\ell_2$ is from material conversion $\ell_1 + \ell_2$ not conversion candidates	event yield
CR HF $\mu$	$\ell\mu\mu$	$\geq 1$	1	$100 < H_T < 300$ GeV $E_T^{\text{miss}} > 35$ GeV total charge = $\pm 1$	$p_T(\ell_3)$
CR HF $e$	$e\ell\ell$	$\geq 1$	1	$\ell_1 + \ell_2$ not conversion candidates $100 < H_T < 275$ GeV $E_T^{\text{miss}} > 35$ GeV total charge = $\pm 1$	$p_T(\ell_3)$
CR $t\bar{t}W^+$	SS $\ell\mu$	$\geq 4$	$\geq 2$	$ \eta(e)  < 1.5$ for $N_b = 2$ : $H_T < 500$ GeV or $N_{\text{jets}} < 6$ for $N_b \geq 3$ : $H_T < 500$ GeV total charge > 0	$N_{\text{jets}}$
CR $t\bar{t}W^-$	SS $\ell\mu$	$\geq 4$	$\geq 2$	$ \eta(e)  < 1.5$ for $N_b = 2$ : $H_T < 500$ GeV or $N_{\text{jets}} < 6$ for $N_b \geq 3$ : $H_T < 500$ GeV total charge < 0	$N_{\text{jets}}$
CR 1b(+)	SS2L+3L	$\geq 4$	1	$\ell_1 + \ell_2$ not from material conversion $H_T > 500$ GeV total charge > 0	$N_{\text{jets}}$
CR 1b(-)	SS2L+3L	$\geq 4$	1	$\ell_1 + \ell_2$ not from material conversion $H_T > 500$ GeV total charge < 0	$N_{\text{jets}}$
VR $t\bar{t}Z$	3L $\ell^\pm\ell^\mp$	$\geq 4$	$\geq 2$	$m_{\ell\ell} \in [81, 101]$ GeV	$N_{\text{jets}}, m_{\ell\ell}$
VR $t\bar{t}W +1b$	SS2L+3L			CR $t\bar{t}W^\pm$    CR 1b( $\pm$ )	$N_{\text{jets}}$
VR $t\bar{t}W +1b+SR$	SS2L+3L			CR $t\bar{t}W^\pm$    CR 1b( $\pm$ )    SR	$N_{\text{jets}}$
SR	SS2L+3L	$\geq 6$	$\geq 2$	$H_T > 500$ GeV $m_{\ell\ell} \notin [81, 101]$ GeV	$H_T$

1079 Most irreducible backgrounds are estimated using MC simulations normalized to their the-  
1080 oretical SM cross sections (template fitting), with the exception of  $t\bar{t}W$  background due to  
1081 MC mismodeling of the process at high jet multiplicities.  
1082 The  $t\bar{t}W$  is instead given four dedicated CRs, and estimated using a data-driven method  
1083 with a fitted function parameterized in  $N_{\text{jets}}$   
1084 All CRs and SR are included in the final LH-fit to data.

### 1085 6.3.1 Template fitting for fake/non-prompt estimation

1086 Template fit method is a semi-data-driven approach that estimates fake/non-prompt back-  
1087 ground distributions by fitting the MC kinematic profiles of background processes arising  
1088 from fake/non-prompt leptons to data.  
1089 Each of the four main sources of fake/non-prompt leptons is assigned a free-floating normal-  
1090 ization factor constrained by a CR enriched with the corresponding background. The NFs  
1091 are determined simultaneously with the signal.

- 1092 •  $\text{NF}_{\text{HF } e(\mu)}$ : events with one reconstructed non-prompt electron (muon) from heavy  
1093 flavor decays,
- 1094 •  $\text{NF}_{\text{Mat. Conv.}}$ : events with one reconstructed non-prompt electrons from photon con-  
1095 version in the detector material
- 1096 •  $\text{NF}_{\text{Low } m_{\gamma^*}}$ : events with one reconstructed non-prompt electrons in an  $e^+e^-$  pair from  
1097 virtual photon ( $\gamma^*$ ) conversion.

### **6.3.2 Charge misidentification data-driven estimation**

The same-sign di-lepton channel in the analysis gives rise to a major background contamination in opposite-sign di-lepton events with one misidentified charge.

Charge misidentification occurs via incorrect track curvature measurements or trident electron contamination from bremsstrahlung, and therefore mainly concerns electrons due to muons' low bremsstrahlung rate and precise curvature information using the ID and MS.

The charge misidentification rates is significant at higher  $p_T$  and varies with  $|\eta|$  as a proxy for the amount of detector material the electron interacted with, and is consequently estimated in this analysis using a data-driven method with assistance from ECIDS.

The charge flip probability  $\epsilon$  is estimated using a sample of  $Z \rightarrow e^+e^-$  events with additional constraints on the invariant mass  $m_{ee}$  to be within 10 GeV of the  $Z$ -boson mass.

The  $Z$ -boson mass window is defined to be within  $4\sigma$  to include most events within the peak, and is determined by fitting the  $m_{ee}$  spectrum of the two leading electrons to a Breit-Wigner function, resulting in a range of [65.57, 113.49] for SS events and [71.81, 109.89] for OS events.

Background contamination near the peak is assumed to be uniform and subtracted using a sideband method.

Since the  $Z$ -boson decay products consist of a pair of opposite-sign electrons, all same-sign electron pairs are considered to be affected by charge misidentification.

Assuming the charge flip probabilities of electrons in an event are uncorrelated, the number of events with same-sign electrons  $N_{ij}^{\text{SS}}$  with the leading electron in the  $i^{\text{th}}$  2D bin in  $(p_T, |\eta|)$  and the sub-leading electron in the  $j^{\text{th}}$  bin can be estimated as

$$N_{ij}^{\text{SS}} = N_{ij}^{\text{tot}}(\epsilon_i(1 - \epsilon_j) + \epsilon_j(1 - \epsilon_i)), \quad (6.1)$$

where  $N_{ij}^{\text{tot}}$  is the total number of events in the  $i^{\text{th}}$  and  $j^{\text{th}}$  bin regardless of charge, and  $\epsilon_{i(j)}$  is the charge flip rate in the  $i^{\text{th}}(j^{\text{th}})$  bin.

Assuming  $N_{ij}^{\text{SS}}$  follows a Poisson distribution around the expectation value  $\bar{N}_{ij}^{\text{SS}}$ , the charge flip rate  $\epsilon$  can be estimated by minimizing a negative-LLH function parameterized in  $p_T$  and  $|\eta|$ ,

$$\begin{aligned} -\ln(\mathcal{L}(\epsilon | N_{\text{SS}})) &= -\ln \prod_{ij} \frac{(N_{ij}^{\text{tot}})^{N_{ij}^{\text{SS}}} \cdot e^{N_{ij}^{\text{tot}}}}{N_{ij}^{\text{SS}}!} \\ &= -\sum_{ij} \left[ N_{ij}^{\text{SS}} \ln(N_{ij}^{\text{tot}}(\epsilon_i(1-\epsilon_j) + \epsilon_j(1-\epsilon_i))) - N_{ij}^{\text{tot}}(\epsilon_i(1-\epsilon_j) + \epsilon_j(1-\epsilon_i)) \right]. \end{aligned} \quad (6.2)$$

$$(6.3)$$

1119 The charge flip rate is then calculated separately for SR and CRs with different electron  
 1120 definitions (CR Low  $m_{\gamma^*}$ , CR Mat. Conv., CR  $t\bar{t}W$ ) using events satisfying 2LSS kinematic  
 1121 selections but with OS electrons, after applying region-specific lepton selections and ECIDS.  
 1122 The following weight is applied to OS events to correct for misidentified SS events within  
 1123 the region:

$$w = \frac{\epsilon_i + \epsilon_j - 2\epsilon_i\epsilon_j}{1 - \epsilon_i - \epsilon_j + 2\epsilon_i\epsilon_j}. \quad (6.4)$$

### 1124 6.3.3 $t\bar{t}W$ background data-driven estimation

1125 -  $t\bar{t}W$  represents a major source of irreducible background contamination in SM and BSM  
 1126 analyses with  $t\bar{t}t\bar{t}$  final states.  
 1127 - Measured cross section for  $t\bar{t}W$  background has been consistently higher than predicted  
 1128 values as seen in previous analyses ( $t\bar{t}H/t\bar{t}W$  multilepton [40][41],  $t\bar{t}t\bar{t}$  analyses [42][16]) due  
 1129 to mismodeling, especially at higher  $N_{\text{jets}}$

<sub>1130</sub> (show postfit  $t\bar{t}W$  VR distribution)

<sub>1131</sub> - Previously, this was handled by assigning large ad-hoc systematic uncertainties to  $t\bar{t}W$   
<sub>1132</sub> events with 7 or more jets. - A semi-data-driven method originally employed in the R-parity-  
<sub>1133</sub> violating-supersymmetry search [43] was used to mitigate this problem. - This method was  
<sub>1134</sub> shown to be effective in the SM  $t\bar{t}t\bar{t}$  observation analysis [**ana:tttt`obs**] by improving  $t\bar{t}W$   
<sub>1135</sub> modeling especially in the showering step and switching  $t\bar{t}W$  systematic uncertainties from  
<sub>1136</sub> predominantly modeling to statistical.

<sub>1137</sub> - MC kinematic distributions for  $t\bar{t}W$  are applied with correction factors obtained from a  
<sub>1138</sub> fitted function parameterized in  $N_{\text{jets}}$ .  
<sub>1139</sub> - The function describes scaling patterns for QCD [44] can be represented by ratio of suc-  
<sub>1140</sub> cessive exclusive jet cross-sections

$$R_{(n+1)/n} = e^{-b} + \frac{\bar{n}}{n+1} = a_0 + \frac{a_1}{1+(j-4)}, \quad (6.5)$$

<sub>1141</sub> where  $n$  is the number of jets in addition to the hard process,  $j$  is the inclusive number of  
<sub>1142</sub> jets, and  $\bar{n}$  is the expectation value for the Poisson distribution for exclusive jet cross-section  
<sub>1143</sub> at jet multiplicity  $n$ , described as  $P_n = \sigma_n / \sigma_{\text{tot}}$ .

<sub>1144</sub> - Same-sign di-lepton  $t\bar{t}W$  events dominate the  $t\bar{t}W$  background and produce 4 jets in the  
<sub>1145</sub> matrix element at tree level for the hard process, so  $n$  is defined starting from 5 jets and  $j$   
<sub>1146</sub> is defined as inclusive number of jets with 4 or more jets, or  $j \equiv n + 4$ .

<sub>1147</sub> - The two terms in the equation correspond respectively to staircase and Poisson scaling  
<sub>1148</sub> between successive multiplicity cross sections, defined as constant ratios  $e^{-b}$  and ratios be-  
<sub>1149</sub> tween Poisson probability for  $n+1$  and  $n$  jets. Staircase scaling is sensitive to events with  
<sub>1150</sub> high jet multiplicity, while Poisson scaling is sensitive to events with low jet multiplicity [44].

1151 - The scaling pattern can then be re-parameterized in  $a_0$  and  $a_1$  to obtain the  $t\bar{t}W$  yield at

1152  $j'$

$$\text{Yield}_{t\bar{t}W(j')} = \text{Yield}_{t\bar{t}W(j=4)} \times \prod_{j=4}^{j'-1} \left( a_0 + \frac{a_1}{1+(j-4)} \right) \quad (6.6)$$

1153 where  $j'$  is defined as  $j' \equiv j+1$  with  $j \geq 4$  since the parameterization starts at the 4<sup>th</sup> jet.

1154 The  $t\bar{t}W$  yield at the 4-jet bin can be represented by a normalization factor applied to  $t\bar{t}W$

1155 MC simulation as  $\text{Yield}_{t\bar{t}W(j=4)} = \text{NF}_{t\bar{t}W(j=4)} \times \text{MC}_{j=4}$ .

1156 To account for the disparity in  $t\bar{t}W^+$  and  $t\bar{t}W^-$  cross-section, assuming the scaling is the

1157 same for both processes,  $\text{NF}_{t\bar{t}W(j=4)}$  can be further split into  $\text{NF}_{t\bar{t}W^+(j=4)}$  and  $\text{NF}_{t\bar{t}W^-(j=4)}$ .

1158 Both NFs are left free-floating to constrain  $t\bar{t}W$  yields at the 4-jet bin in CR 1b(+) and CR

1159 1b(-).

1160 The final  $N_{\text{jets}}$ -parameterized function can then be represented by  $\text{NF}_{t\bar{t}W(j')}$  as

$$\text{NF}_{t\bar{t}W(j')} = \left( \text{NF}_{t\bar{t}W^+(j=4)} + \text{NF}_{t\bar{t}W^-(j=4)} \right) \times \prod_{j=4}^{j'-1} \left( a_0 + \frac{a_1}{1+(j-4)} \right). \quad (6.7)$$

1161 This normalization is calculated and applied separately for each sub-sample of  $t\bar{t}W^+$  and

1162  $t\bar{t}W^-$  in an  $N_{\text{jets}}$  bin for  $4 \leq N_{\text{jets}} < 10$ .

1163 Due to small contributions in the CRs, events with  $N_{\text{jets}} < 4$  and  $N_{\text{jets}} \geq 10$  are not

1164 normalized with this scheme.

1165 Instead,  $N_{\text{jets}} < 4$   $t\bar{t}W$  events are fitted by propagating normalization in the 4-jet bin

1166 without additional shape correction. The correction factor for  $t\bar{t}W$  events with  $N_{\text{jets}} \geq$

1167 10 is obtained by summing up the overflow from  $N_{\text{jets}} = 10$  to  $N_{\text{jets}} = 12$ , described as

1168  $\sum_{j'=10}^{12} \prod_{j=4}^{j'-1} \left( a_0 + \frac{a_1}{1+(j-4)} \right)$ . Events with  $N_{\text{jets}} \geq 13$  are negligible and thus not included

1169 in the sum.

<sub>1170</sub> **Control region definitions**

<sub>1171</sub> Four control regions CR  $t\bar{t}W^+$ , CR  $t\bar{t}W^-$ , CR 1b(+), CR 1b(-) are constructed to fit

<sub>1172</sub> NF  $t\bar{t}W^{\pm}(j=4)$  and the scaling parameters  $a_0$ ,  $a_1$  for the  $t\bar{t}W$  background, as well as vali-

<sub>1173</sub> dating the parameterization.

<sub>1174</sub> Events in CR  $t\bar{t}W^{\pm}$  are required to contain at least two  $b$ -tagged jets similar to the SR to

<sub>1175</sub> determine the  $t\bar{t}W$  normalization within an SR-related phase space. Orthogonality with SR

<sub>1176</sub> is satisfied by requiring  $H_T < 500$  GeV or  $N_{\text{jets}} < 6$  when  $N_b = 2$ , and  $H_T < 500$  GeV when

<sub>1177</sub>  $N_b \geq 3$ .

<sub>1178</sub> The remaining CR 1b( $\pm$ ) require events to have  $H_T > 500$  GeV and at least four jets to

<sub>1179</sub> encompass events with high  $N_{\text{jets}}$ , which can be used to determine the  $t\bar{t}W$  jet multiplici-

<sub>1180</sub> ty spectrum for fitting  $a_{0,1}$ . The selection criteria also include exactly one  $b$ -tagged jet to

<sub>1181</sub> maintain orthogonality with SR. Assuming the  $t\bar{t}W$  jet multiplicity distribution is similar

<sub>1182</sub> across different  $N_b$ , a fitted  $N_{\text{jets}}$  distribution in CR 1b( $\pm$ ) can be used to describe the  $t\bar{t}W$

<sub>1183</sub> parameterization at higher  $N_{\text{jets}}$ . The full selection criteria for all four regions are shown in

<sub>1184</sub> ??

<sub>1185</sub>

<sub>1186</sub> Validating the  $t\bar{t}W$  parameterization in Equation 6.7 makes use of the unique charge

<sub>1187</sub> asymmetry in  $t\bar{t}W$  production that's not present in other background or signal processes.

<sub>1188</sub> The number of events with all negatively charged leptons is subtracted from that of events

<sub>1189</sub> with all positively charged leptons, which cancels out charge symmetric events and leaves

<sub>1190</sub> the  $t\bar{t}W$  background. Validation is done via a statistical-only (stat-only) fit to the  $t\bar{t}W$  MC

<sub>1191</sub> prediction in CR 1b( $\pm$ ).

# 1192 Chapter 7. Systematic Uncertainties

1193 (nuisance parameters)

1194 - Heavy pruning, 5% on shape and normalization pruning (to fit timeline?)

## 1195 7.1 Experimental uncertainties

1196 Instrumental & minor:

1197 - uncertainty on the integrated luminosity of the 2015-2018 Run 2 data set is 0.83%, obtained

1198 by the LUCID-2 detector for the primary luminosity measurements complemeted by the ID

1199 and calorimeters

1200 - Pile-up modeling in MC was calibrated to data through pile-up reweighting, resulting in a  
1201 set of calibration SFs and associated uncertainties.

1202 In general, calibrating MC simulations to match performance in data incurs uncertainties

1203 associated with the MC-to-data scale factors obtained from the calibration, which are in

1204 turn propagated to observables in the analysis.

### 1205 7.1.1 Leptons

1206 The trigger/reconstruction/ID/isolation efficiencies of electrons and muons (with separate  
1207 systematic and statistical components for muon) differ between MC simulation and data,  
1208 and require correction in the form of SFs with its associated uncertainties.

1209 Similarly, electron and muon energy-momentum scale and resolution also incur uncertainties  
1210 from MC-to-data correction, calculated by varying scale and resolution during simulations.

1211 Muons have additional uncertainties for charge-dependent and charge-independent momen-

1212 tum scale, and detector-specific (ID, MS, CB) track resolution.

1213 The charge identification/ECIDS efficiency also gives rise to an additional uncertainty com-

1214 ponent.

1215

### 1216 7.1.2 Jets

1217 Experimental uncertainties on jets are dominated by flavor tagging-related uncertainties,

1218 with subleading contributions from jet energy scale/resolution (JES/JER) and NNJvt cali-

1219 bration.

1220

#### 1221 Jet energy scale

1222 JES and its associated uncertainties are determined using data from test-beam and LHC

1223 collisions and MC simulated samples, decomposed into uncorrelated components:

- 1224 • Effective nuisance parameters (NPs): 15  $p_T$ -dependent uncertainty components in total  
1225 measured in situ, grouped based on their origin (2 detector-related, 4 modeling-related,  
1226 3 mixed, 6 statistical-related)

- 1227 •  $\eta$  intercalibration: 6 total components (1 modeling-related, 4 non-closure and 1 statistical-  
1228 related) associated with the correction of the forward jets' ( $0.8 \leq |\eta| < 4.5$ ) energy  
1229 scale to that of the central jets ( $|\eta| < 0.8$ ).

- 1230 • Flavor composition/response: 2 components for relative quark-gluon flavor composi-  
1231 tions in background and signal samples, and 2 components for uncertainty in responses  
1232 to gluon-initiated versus quark-initiated jets

- Pile-up subtraction: 4 components, two for uncertainty in  $\mu$  (`OffsetMu`) and  $N_{PV}$  (`OffsetNPV`) modeling, one for residual  $p_T$ -dependency (`PtTerm`) and one for topology dependence on the per-event  $p_T$  density modeling (`RhoTopology`)
- Punch-through effect treatment: two terms (AF3 fast simulation and full detector simulations) for GSC punch-through jet response correction between data and MC.
- Non-closure: one term to account for difference between AF3-simulated samples and full detector simulations.
- High- $p_T$  single-particle response: one term for response to high- $p_T$  jets from single-particle and test-beam measurements
- $b$ -jets response: one term for uncertainty in the response to  $b$ -jets

## 1243 Jet energy resolution

1244 JER measured separately in data and MC simulations using in situ techniques as a function  
 1245 of  $p_T$  and  $\eta$  for a given jet. Associated uncertainties are defined as quadratic difference  
 1246 between data and MC simulations.  
 1247 This analysis uses the full JER uncertainty set provided for Run 2 searches with 14 total com-  
 1248 ponents: 12 effective NPs and 2 for difference between data and MC simulation, separately  
 1249 for AF3 and FS.

## 1250 Jet vertex tagging

1251 JVT associated uncertainty is obtained by varying the JVT efficiency correction SFs within  
 1252 their range of uncertainty. This uncertainty accounts for remaining contamination from  
 1253 pile-up jets after applying pile-up suppression and MC generator choice.

1254 **Flavor tagging**

1255 SFs for  $b$ -jets tagging efficiencies and  $c$ -/light-jets mis-tagging rates are obtained as a function  
1256 of  $p_T$  for  $b$ -/ $c$ -/light-jets and PCB scores. The covariance matrix of systematic and statistical  
1257 uncertainties is diagonalized and reduced in dimensions using principle component analysis  
1258 (PCA), resulting in a set of orthogonal NPs: 85 for  $b$ -jets, 56 for  $c$ -jets and 42 for light-jets.

1259 **7.1.3 Missing transverse energy**

1260 Uncertainties for  $E_T^{\text{miss}}$  arise from possible miscalibration of its soft-track component, and  
1261 are estimated using data-MC comparison of the  $p_T$  scale and resolution between the hard  
1262 and soft  $E_T^{\text{miss}}$  terms. These uncertainties are represented by three independent terms: one  
1263 for scale uncertainty and two resolution uncertainties for the parallel and perpendicular  
1264 components.

1265 **7.2 Modeling uncertainties**

1266 **7.2.1 Signal and irreducible background uncertainties**

1267 - scale variations - 6-point variation method, varying  $\mu_R$  &  $\mu_F$  vs central values to cover  
1268 missing higher-order QCD corrections (signal & all major irreducible background)  
1269  $(\mu_R, \mu_F) = (0.5, 0.5), (0.5, 1), (1, 0.5), (1, 2), (2, 1), (2, 2)$  - pdf uncertainty: flat 1% for  $t\bar{t}Z'$ ,  
1270  $t\bar{t}t\bar{t}$ ,  $t\bar{t}Z$ ,  $t\bar{t}H$ , envelope of differences between nominal vs. other pdf choices for  $t\bar{t}t$

1271  **$t\bar{t}Z'$  signal**

1272 - parton distribution function: 1%

Table 7.1: Summary of the experimental systematic uncertainties considered in this analysis.

Systematic uncertainty	Terms	Scale [%]
<b>Event</b>		
Luminosity	1	0.83
Pile-up reweighting	1	$\mathcal{O}(1) \sim \mathcal{O}(10)$
<b>Electrons</b>		
Trigger efficiency	1	$\mathcal{O}(10^{-2}) \sim \mathcal{O}(10^{-1})$
Reconstruction efficiency <sup>†</sup>	1	$\mathcal{O}(10^{-1}) \sim \mathcal{O}(1)$
Identification efficiency <sup>†</sup>	1	$\mathcal{O}(10^{-1}) \sim \mathcal{O}(1)$
Isolation efficiency <sup>†</sup>	1	$\mathcal{O}(10^{-1}) \sim \mathcal{O}(1)$
Energy scale	1	$\mathcal{O}(10^{-2}) \sim \mathcal{O}(10^{-1})$
Energy resolution	1	$\mathcal{O}(10^{-2}) \sim \mathcal{O}(10^{-1})$
Charge identification (ECIDS) efficiency <sup>†</sup>	1	$\mathcal{O}(10^{-1}) \sim \mathcal{O}(1)$
<b>Muons</b>		
Trigger efficiency (stat/sys)	2	$\mathcal{O}(10^{-1}) \sim \mathcal{O}(1)$
Track-to-vertex association efficiency (stat/sys)	2	$\mathcal{O}(10^{-2}) \sim \mathcal{O}(10^{-1})$
Reconstruction/identification efficiency (stat/sys)	2	$\mathcal{O}(10^{-1}) \sim \mathcal{O}(1)$
Low- $p_T$ ( $< 15$ GeV) reconstruction/identification efficiency (stat/sys)	2	$\mathcal{O}(10^{-1}) \sim \mathcal{O}(1)$
Isolation efficiency (stat/sys)	2	$\mathcal{O}(10^{-1}) \sim \mathcal{O}(1)$
Charge-independent momentum scale	1	$\mathcal{O}(10^{-2}) \sim \mathcal{O}(10^{-1})$
Charge-dependent momentum scale	4	$\mathcal{O}(10^{-2}) \sim \mathcal{O}(10^{-1})$
Energy resolution (CB)	1	$\mathcal{O}(10^{-2}) \sim \mathcal{O}(10^{-1})$
Energy resolution (ID & MS)*	2	$\mathcal{O}(10^{-2}) \sim \mathcal{O}(10^{-1})$
<b>Jets</b>		
JES effective NP	15	$\mathcal{O}(10^{-2}) \sim \mathcal{O}(1)$
JES $\eta$ intercalibration	3	$\mathcal{O}(10^{-1}) \sim \mathcal{O}(1)$
JES flavor composition	2	$\mathcal{O}(10^{-1}) \sim \mathcal{O}(1)$
JES flavor response	1	$\mathcal{O}(10^{-1}) \sim \mathcal{O}(1)$
JES pile-up	4	$\mathcal{O}(10^{-1}) \sim \mathcal{O}(10)$
JES punch-through (FS/AF3*)	2	$< \mathcal{O}(10^{-2})$
JES non-closure	1	$\mathcal{O}(10^{-2}) \sim \mathcal{O}(10^{-1})$
JES high- $p_T$ single particle	1	$< \mathcal{O}(10^{-2})$
JES $b$ -jet response	1	$\mathcal{O}(10^{-1}) \sim \mathcal{O}(1)$
JER effective NP	12	$\mathcal{O}(10^{-1}) \sim \mathcal{O}(1)$
JER data/MC (FS/AF3*)	2	$\mathcal{O}(10^{-1}) \sim \mathcal{O}(1)$
JVT efficiency	1	$\mathcal{O}(10^{-1}) \sim \mathcal{O}(1)$
GN2v01 $b$ -tagging efficiency ( $b$ -jets)	85	$\mathcal{O}(10^{-2}) \sim \mathcal{O}(1)$
GN2v01 $b$ -tagging efficiency ( $c$ -jets)	56	$\mathcal{O}(10^{-2}) \sim \mathcal{O}(1)$
GN2v01 $b$ -tagging efficiency (light-jets)	42	$\mathcal{O}(10^{-2}) \sim \mathcal{O}(1)$
<b><math>E_T^{\text{miss}}</math>-Terms</b>		
Track-based soft term for transversal resolution	1	$\mathcal{O}(10^{-2}) \sim \mathcal{O}(10^{-1})$
Track-based soft term for longitudinal resolution	1	$\mathcal{O}(10^{-2}) \sim \mathcal{O}(10^{-1})$
Track-based soft term for longitudinal scale	1	$\mathcal{O}(10^{-2}) \sim \mathcal{O}(10^{-1})$

<sub>1273</sub> **SM  $t\bar{t}t\bar{t}$  background**

<sub>1274</sub> - cross section: 20% from NLO prediction in QCD+EW

<sub>1275</sub> - generator uncertainty: madgraph5\_amc@nlo (nominal) vs sherpa 2.2.10

<sub>1276</sub> - parton shower uncertainty: pythia8 (nominal) vs herwig7

<sub>1277</sub> **SM  $t\bar{t}t$  background**

<sub>1278</sub> - cross section: 30% from NLO prediction in QCD+EW

<sub>1279</sub> - additional  $b$ -jets: 50% for  $t\bar{t}t$  events with 4+ truth  $b$ -jets

<sub>1280</sub>  **$t\bar{t}W$ ,  $t\bar{t}Z$ ,  $t\bar{t}H$  background**

<sub>1281</sub> - cross section:  $t\bar{t}Z$  12%,  $t\bar{t}H$  10% (**from CERN yellow report**)

<sub>1282</sub> no cross-section and pdf uncertainties for  $t\bar{t}W$  since normalizations and jet multiplicity spec-

<sub>1283</sub> trum are estimated with data-driven method

<sub>1284</sub> - parton shower uncertainty:  $t\bar{t}H$  powhegbox+pythia8 (nominal) vs powhegbox+herwig7

<sub>1285</sub> - additional  $b$ -jets: events with additional HF jets can contaminate SR and are challenging

<sub>1286</sub> to model w/ MC - 50% for events with an additional truth  $b$ -jet not from top-quark decay,

<sub>1287</sub> additional 50% for 2 or more

<sub>1288</sub> - generator uncertainty **table?**

<sub>1289</sub> •  $t\bar{t}W$ - sherpa (nominal) vs madgraph5\_amc@nlo

<sub>1290</sub> •  $t\bar{t}Z$ - madgraph5\_amc@nlo (nominal) vs sherpa 2.2.10

<sub>1291</sub> •  $t\bar{t}H$ - powheg8/PhPy8 (nominal) vs powheg8/PhPy8 pthard

<sub>1292</sub> **Other backgrounds**

- <sub>1293</sub> •  $t(\bar{t})X$ : cross section 30%
- <sub>1294</sub> •  $VV$ : cross section (STDM-2018-03) uncorrelated 20%/50%/60% for events with 3-  
<sub>1295</sub> /4/5+ jets; events with 1+ truth  $b$ -jets not from top decay 50%
- <sub>1296</sub> •  $t\bar{t}VV, VVV, VH$ : cross section 50%; additional  $b$ -jets same as  $VV$

<sub>1297</sub> **7.2.2 Reducible background uncertainties**

- <sub>1298</sub> • Electron charge misidentification background:
- <sub>1299</sub> • Material and internal (low  $\gamma^*$ ) conversion background: estimated based on data/MC  
<sub>1300</sub> differences in a region enriched with  $Z \rightarrow \ell^+\ell^-\gamma$ ; 30% & 21% for material & internal  
<sub>1301</sub> conversion
- <sub>1302</sub> • Heavy-flavor non-prompt lepton background: estimated based on data/MC differences  
<sub>1303</sub> in CR/SR distributions, ranging from 20-100%
- <sub>1304</sub> • Light-flavor decays and other fake/non-prompt background: Conservative normal-  
<sub>1305</sub> ization uncertainty of 100% for light-flavor non-prompt lepton background (ATLAS-  
<sub>1306</sub> CONF-2019-045), 30% for normalization of all other fake backgrounds.
- <sub>1307</sub> • +HF: contaminates SR phase space with large  $b$ -jet multiplicity, estimated  
<sub>1308</sub> from data/MC discrepancy, 30% for events with

Table 7.2: Caption

Systematic uncertainty	Terms	Scale [%]
<b><math>t\bar{t}Z'</math> modeling</b>		
Renormalization & factorization scale		
PDF		
<b>SM <math>t\bar{t}\bar{t}</math> modeling</b>		
Cross-section		
Renormalization & factorization scale		
PDF		
Generator choice		
Parton shower model		
<b>SM <math>t\bar{t}t</math> modeling</b>		
Cross-section		
Renormalization & factorization scale		
PDF		
Additional $b$ -jets		
<b><math>t\bar{t}W</math> modeling</b>		
Renormalization & factorization scale		
Generator choice		
Additional $b$ -jets		
<b><math>t\bar{t}Z</math> modeling</b>		
Cross-section		
Renormalization & factorization scale		
PDF		
Generator choice		
Additional $b$ -jets		
<b><math>t\bar{t}H</math> modeling</b>		
Cross-section		
Renormalization & factorization scale		
PDF		
Generator choice		
Parton shower model		
Additional $b$ -jets		
<b>Other background modeling</b>		
Cross-section		
Additional $b$ -jets		

Table 7.3: Caption

Systematic uncertainty	Terms	Scale [%]
<b>Reducible SM background</b>		
$t\bar{t}/V/t+\text{jets}$	2	
Charge misidentification	1	
<b>Fake &amp; non-prompt background</b>		
Low $\gamma^*$	1	
Material conversion	1	
HF $e$	1	
HF $\mu$	1	
Light-flavor decays	1	100
Other fakes	1	30

<sub>1309</sub> **Chapter 8. Results**

<sub>1310</sub> **8.1 Statistical model**

<sub>1311</sub> **8.1.1 Binned profile likelihood fit**

<sub>1312</sub> **8.1.2 Signal significance**

<sub>1313</sub> **8.1.3 Limit exclusion**

<sub>1314</sub> **8.2 Fit results**

<sub>1315</sub> Fit setup

- <sub>1316</sub> • Plain Asimov fit (**only mentioning briefly**): all regions included; simulated data used in the fit match exactly to MC prediction with nominal  $\mu_{t\bar{t}Z'}$  set to 0 and allowed to free-float.

<sub>1319</sub> Purpose: to perform studies on optimizing fitted parameters and expected sensitivity; refining background estimation techniques; optimizing region definition and object definition

- <sub>1322</sub> • Real SRs-blinded fit: similar to plain Asimov, but use observed data in CRs.

<sub>1323</sub> Purpose: study the behavior of background estimation using real observed data in CRs on Asimov data in SRs and assessing the influence of statistical effects on fitted parameters and expected sensitivity

- <sub>1326</sub> • Real SRs-unblinded/ $H_T$  fit: all regions included,

<sub>1327</sub> **8.3 Limits**

1328 Chapter 9. Summary

# <sup>1329</sup> References

- <sup>1330</sup> [1] C. Burgard and D. Galbraith. *Standard Model of Physics*. URL: <https://texample.net/model-physics/> (visited on 06/02/2025) (cit. on p. 4).
- <sup>1331</sup>
- <sup>1332</sup> [2] A. Pich. *The Standard Model of electroweak interactions. 2004 European School of High-Energy Physics*. Feb. 2005, pp. 1–48. arXiv: [hep-ph/0502010 \[hep-ex\]](https://arxiv.org/abs/hep-ph/0502010) (cit. on p. 12).
- <sup>1333</sup>
- <sup>1334</sup>
- <sup>1335</sup> [3] P. Higgs. *Broken symmetries and the masses of gauge bosons*. *Phys. Rev. Lett.* **13** (16 1964), pp. 508–509 (cit. on p. 13).
- <sup>1336</sup>
- <sup>1337</sup> [4] P. Higgs. *Broken symmetries, massless particles and gauge fields*. *Physics Letters* **12.2** (1964), pp. 132–133. ISSN: 0031-9163 (cit. on p. 13).
- <sup>1338</sup>
- <sup>1339</sup> [5] F. Englert and R. Brout. *Broken Symmetry and the Mass of Gauge Vector Mesons*. *Phys. Rev. Lett.* **13** (9 1964), pp. 321–323 (cit. on p. 13).
- <sup>1340</sup>
- <sup>1341</sup> [6] ATLAS Collaboration. *Observation of a new particle in the search for the Standard Model Higgs boson with the ATLAS detector at the LHC*. *Phys. Lett. B* **716** (2012), p. 1. arXiv: [1207.7214 \[hep-ex\]](https://arxiv.org/abs/1207.7214) (cit. on p. 13).
- <sup>1342</sup>
- <sup>1343</sup>

- 1344 [7] CMS Collaboration. *Observation of a new boson at a mass of 125 GeV with the CMS*  
1345 *experiment at the LHC*. *Phys. Lett. B* 716 (2012), p. 30. arXiv: 1207.7235 [hep-ex]  
1346 (cit. on p. 13).
- 1347 [8] J. Ellis. *Higgs Physics. 2013 European School of High-Energy Physics*. 2015, pp. 117–  
1348 168. arXiv: 1312.5672 [hep-ph] (cit. on pp. 14, 15).
- 1349 [9] P. Langacker. *The Physics of Heavy  $Z'$  Gauge Bosons*. *Rev. Mod. Phys.* 81 (2009),  
1350 pp. 1199–1228. arXiv: 0801.1345 [hep-ph] (cit. on p. 16).
- 1351 [10] G. Ferretti and D. Karateev. *Fermionic UV completions of composite Higgs models*.  
1352 *Journal of High Energy Physics* 2014.3 (Mar. 2014). ISSN: 1029-8479. URL: [http://dx.doi.org/10.1007/JHEP03\(2014\)077](http://dx.doi.org/10.1007/JHEP03(2014)077) (cit. on p. 16).
- 1354 [11] L. Vecchi. *A dangerous irrelevant UV-completion of the composite Higgs*. *JHEP* 02  
1355 (2017), p. 094. arXiv: 1506.00623 [hep-ph] (cit. on p. 16).
- 1356 [12] K. Agashe, A. Delgado, M. J. May, and R. Sundrum. *RS1, custodial isospin and*  
1357 *precision tests*. *JHEP* 08 (2003), p. 050. arXiv: hep-ph/0308036 [hep-ph] (cit. on  
1358 p. 16).
- 1359 [13] K. Agashe, R. Contino, and A. Pomarol. *The Minimal composite Higgs model*. *Nucl.*  
1360 *Phys. B* 719 (2005), pp. 165–187. arXiv: hep-ph/0412089 [hep-ph] (cit. on p. 16).
- 1361 [14] N. Greiner, K. Kong, J.-C. Park, S. C. Park, and J.-C. Winter. *Model-independent*  
1362 *production of a top-phobic resonance at the LHC*. *Journal of High Energy Physics* 2015.4  
1363 (2015), p. 29. ISSN: 1029-8479 (cit. on pp. 17, 18).
- 1364 [15] J. H. Kim, K. Kong, S. J. Lee, and G. Mohlabeng. *Probing TeV scale top-phobic reso-*  
1365 *nances with boosted top-tagging at the high luminosity LHC*. *Phys. Rev. D* 94 (3 2016),  
1366 p. 035023 (cit. on p. 17).

- 1367 [16] ATLAS Collaboration. *Observation of four-top-quark production in the multilepton*  
1368 *final state with the ATLAS detector.* Eur. Phys. J. C 83 (2023), p. 496. arXiv: 2303.  
1369 15061 [hep-ex] (cit. on pp. 19, 61).
- 1370 [17] High Luminosity LHC Project Organization. *The HL-LHC project.* URL: <https://hilumilhc.web.cern.ch/content/hl-lhc-project> (visited on 06/11/2025) (cit. on p. 22).
- 1372 [18] ATLAS Collaboration. *Standard Model Summary Plots October 2023.* ATL-PHYS-  
1373 PUB-2023-039. 2023. URL: <https://cds.cern.ch/record/2882448> (cit. on p. 23).
- 1374 [19] ATLAS Collaboration. *Topological cell clustering in the ATLAS calorimeters and its*  
1375 *performance in LHC Run 1.* Eur. Phys. J. C 77 (2017), p. 490. arXiv: 1603.02934  
1376 [hep-ex] (cit. on p. 34).
- 1377 [20] W. Lampl et al. *Calorimeter clustering algorithms: description and performance.* ATL-  
1378 LARG-PUB-2008-002. 2008. URL: <https://cds.cern.ch/record/1099735> (cit. on p. 34).
- 1379 [21] ATLAS Collaboration. *Performance of the ATLAS track reconstruction algorithms in*  
1380 *dense environments in LHC Run 2.* Eur. Phys. J. C 77 (2017), p. 673. arXiv: 1704.07983  
1381 [hep-ex] (cit. on p. 35).
- 1382 [22] T. Cornelissen et al. *Concepts, design and implementation of the ATLAS New Tracking*  
1383 (*NEWT*). Tech. rep. Geneva: CERN, 2007. URL: <https://cds.cern.ch/record/1020106>  
1384 (cit. on p. 36).
- 1385 [23] R. Frühwirth. *Application of Kalman filtering to track and vertex fitting.* Nucl. Instrum.  
1386 Methods Phys. Res. A 262.2 (1987), pp. 444–450. ISSN: 0168-9002 (cit. on p. 36).
- 1387 [24] T. Cornelissen et al. *The global  $\chi^2$  track fitter in ATLAS.* Journal of Physics: Confer-  
1388 ence Series 119.3 (2008), p. 032013 (cit. on p. 36).

- 1389 [25] ATLAS Collaboration. *Improved electron reconstruction in ATLAS using the Gaussian*  
1390 *Sum Filter-based model for bremsstrahlung*. ATLAS-CONF-2012-047. 2012. URL: <https://cds.cern.ch/record/1449796> (cit. on p. 36).
- 1391  
1392 [26] D. Wicke. *A new algorithm for solving tracking ambiguities*. Tech. rep. Oct. 1998. URL:  
1393 <https://cds.cern.ch/record/2625731> (cit. on p. 36).
- 1394 [27] A. Salzburger and on behalf of the ATLAS Collaboration. *Optimisation of the ATLAS*  
1395 *Track Reconstruction Software for Run-2*. *Journal of Physics: Conference Series* 664.7  
1396 (2015), p. 072042 (cit. on p. 36).
- 1397 [28] ATLAS Collaboration. *Measurements of b-jet tagging efficiency with the ATLAS de-*  
1398 *tector using  $t\bar{t}$  events at  $\sqrt{s} = 13 \text{ TeV}$* . *JHEP* 08 (2018), p. 089. arXiv: [1805.01845](https://arxiv.org/abs/1805.01845)  
1399 [[hep-ex](#)] (cit. on p. 39).
- 1400 [29] ATLAS Collaboration. *Graph Neural Network Jet Flavour Tagging with the ATLAS*  
1401 *Detector*. ATL-PHYS-PUB-2022-027. 2022. URL: <https://cds.cern.ch/record/2811135>  
1402 (cit. on p. 40).
- 1403 [30] A. Duperrin. *Flavour tagging with graph neural networks with the ATLAS detector*.  
1404 Tech. rep. Presented at DIS2023, Michigan State University, USA. Geneva: CERN,  
1405 2023. arXiv: [2306.04415](https://arxiv.org/abs/2306.04415) [[hep-ex](#)]. URL: <https://cds.cern.ch/record/2860610> (cit. on  
1406 p. 40).
- 1407 [31] S. Van Stroud et al. *FTAG Run-3 Algorithms Performance*. Tech. rep. Geneva: CERN,  
1408 2023. URL: <https://cds.cern.ch/record/2872884> (cit. on p. 40).
- 1409 [32] ATLAS Collaboration. *Electron reconstruction and identification in the ATLAS exper-*  
1410 *iment using the 2015 and 2016 LHC proton–proton collision data at  $\sqrt{s} = 13 \text{ TeV}$* .

- 1411 Eur. Phys. J. C 79 (2019), p. 639. arXiv: 1902.04655 [physics.ins-det] (cit. on  
1412 pp. 41–44).
- 1413 [33] ATLAS Collaboration. *Electron and photon performance measurements with the AT-*  
1414 *LAS detector using the 2015–2017 LHC proton–proton collision data*. JINST 14 (2019),  
1415 P12006. arXiv: 1908.00005 [hep-ex] (cit. on pp. 41, 43–45).
- 1416 [34] ATLAS Collaboration. *Electron Identification with a Convolutional Neural Network in*  
1417 *the ATLAS Experiment*. ATL-PHYS-PUB-2023-001. 2023. URL: <https://cds.cern.ch/record/2850666> (cit. on p. 44).
- 1419 [35] ATLAS Collaboration. *Muon reconstruction and identification efficiency in ATLAS*  
1420 *using the full Run 2 pp collision data set at  $\sqrt{s} = 13 \text{ TeV}$* . Eur. Phys. J. C 81 (2021),  
1421 p. 578. arXiv: 2012.00578 [hep-ex] (cit. on pp. 46, 47).
- 1422 [36] ATLAS Collaboration. *Muon reconstruction performance of the ATLAS detector in*  
1423 *proton–proton collision data at  $\sqrt{s} = 13 \text{ TeV}$* . Eur. Phys. J. C 76 (2016), p. 292. arXiv:  
1424 1603.05598 [hep-ex] (cit. on p. 46).
- 1425 [37] ATLAS Collaboration. *Performance of missing transverse momentum reconstruction*  
1426 *with the ATLAS detector using proton–proton collisions at  $\sqrt{s} = 13 \text{ TeV}$* . Eur. Phys.  
1427 J. C 78 (2018), p. 903. arXiv: 1802.08168 [hep-ex] (cit. on p. 47).
- 1428 [38] ATLAS Collaboration.  *$E_T^{\text{miss}}$  performance in the ATLAS detector using 2015–2016*  
1429 *LHC pp collisions*. ATLAS-CONF-2018-023. 2018. URL: <https://cds.cern.ch/record/2625233> (cit. on p. 48).
- 1431 [39] ATLAS Collaboration. *Observation of electroweak production of two jets in association*  
1432 *with an isolated photon and missing transverse momentum, and search for a Higgs*

- 1433 *boson decaying into invisible particles at 13 TeV with the ATLAS detector.* *Eur. Phys.*
- 1434 *J. C* **82** (2022), p. 105. arXiv: 2109.00925 [hep-ex] (cit. on p. 49).
- 1435 [40] ATLAS Collaboration. *Analysis of  $t\bar{t}H$  and  $t\bar{t}W$  production in multilepton final states*
- 1436 *with the ATLAS detector.* ATLAS-CONF-2019-045. 2019. URL: <https://cds.cern.ch/record/2693930> (cit. on p. 61).
- 1437
- 1438 [41] ATLAS Collaboration. *Measurement of the total and differential cross-sections of  $t\bar{t}W$*
- 1439 *production in  $pp$  collisions at  $\sqrt{s} = 13$  TeV with the ATLAS detector.* *JHEP* **05** (2024),
- 1440 p. 131. arXiv: 2401.05299 [hep-ex] (cit. on p. 61).
- 1441 [42] ATLAS Collaboration. *Evidence for  $t\bar{t}t\bar{t}$  production in the multilepton final state in*
- 1442 *proton–proton collisions at  $\sqrt{s} = 13$  TeV with the ATLAS detector.* *Eur. Phys. J. C* **80**
- 1443 (2020), p. 1085. arXiv: 2007.14858 [hep-ex] (cit. on p. 61).
- 1444 [43] ATLAS Collaboration. *Search for R-parity-violating supersymmetry in a final state*
- 1445 *containing leptons and many jets with the ATLAS experiment using  $\sqrt{s} = 13$  TeV*
- 1446 *proton–proton collision data.* *Eur. Phys. J. C* **81** (2021), p. 1023. arXiv: 2106.09609
- 1447 [hep-ex] (cit. on p. 62).
- 1448 [44] E. Gerwick, T. Plehn, S. Schumann, and P. Schichtel. *Scaling Patterns for QCD Jets.*
- 1449 *JHEP* **10** (2012), p. 162. arXiv: 1208.3676 [hep-ph] (cit. on p. 62).